

Pressure torque of torsional Alfvén modes acting on an ellipsoidal mantle

F. Gerick^{1,2}, D. Jault¹, J. Noir² and J. Vidal³

¹ Univ. Grenoble Alpes, Univ. Savoie Mont Blanc, CNRS, IRD, IFSTTAR, ISTerre, 38000 Grenoble, France.

² Institute of Geophysics, ETH Zurich, Zurich, Switzerland

³ Department of Applied Mathematics, School of Mathematics, University of Leeds, Leeds, LS2 9JT, United Kingdom

22 April 2020

SUMMARY

We investigate the pressure torque between the fluid core and the solid mantle arising from magnetohydrodynamic modes in a rapidly rotating planetary core. A two-dimensional reduced model of the core fluid dynamics is developed to account for the non-spherical core-mantle boundary. The simplification of such a quasi-geostrophic model rests on the assumption of invariance of the equatorial components of the fluid velocity along the rotation axis. We use this model to investigate and quantify the axial torques of linear modes, focusing on the torsional Alfvén modes (TM) in an ellipsoid. We verify that the periods of these modes do not depend on the rotation frequency. Furthermore, they possess angular momentum resulting in a net pressure torque acting on the mantle. This torque scales linearly with the equatorial ellipticity. We estimate that for the TM calculated here topographic coupling to the mantle is too weak to account for the variations in the Earth’s length-of-day.

Key words: Core; Earth rotation variations; Numerical modelling

1 INTRODUCTION

Decadal variations in the Earth’s length-of-day (LOD) have long been associated with dynamics in the liquid outer core (Munk & MacDonald 1960; Hide 1966; Jault et al. 1988; Gross 2015). More specifically, a pronounced variation on a period of roughly six years cannot be explained by atmospheric, oceanic and tidal forces, which are responsible for LOD variations on shorter time scales (Abarca del Rio et al. 2000; Holme & de Viron 2013). Torsional Alfvén modes (TM) in the outer core, first studied by Braginsky (1970), have been proposed later as the origin of the six year variation in the LOD (Gillet et al. 2010). In the sphere, these oscillations consist of differentially rotating nested geostrophic cylinders, stretching and shearing the magnetic field lines. Recent advances in magnetic field observations and inverse modelling of the outer core flow at the core-mantle boundary (CMB) have revealed recurring TM with 4-year travel time through the Earth’s outer core (Gillet et al. 2010, 2015). Gillet et al. (2017) investigated the LOD variations that result from the TM propagation, assuming that the only stresses between the core and the mantle are electromagnetic. Relying on the study of Schaeffer & Jault (2016), they inferred constraints on the electrical conductivity of the lowermost mantle. To account for the observed LOD variations, a conductance of the lowermost mantle of $3 \times 10^7 - 10^8$ S is needed (Gillet et al. 2017). Another mechanism of coupling

outer core dynamics to the solid mantle is through gravitational coupling between a deformed inner core and a non-spherical CMB (Buffett 1996a,b; Mound & Buffett 2006). A phase lag between the deformations leads to a torque on the mantle. Even though recent advances in atmospheric and oceanic tide modelling have improved the isolation of gravitational signals from core dynamics, the measurements are still inconclusive (Davies et al. 2014; Watkins et al. 2018).

The third mechanism, investigated here, that may account for exchange of angular momentum between core and mantle is topographic coupling. It has long been proposed that, for a non-spherical CMB, there could be a significant pressure torque exerted by flows in the outer core (Hide 1969). The fluid pressure should scale as $\rho\Omega UR_0$, where ρ is the core density, Ω the angular speed of the Earth’s rotation, U a typical horizontal velocity and R_0 the core radius. A typical amplitude of $\mathcal{O}(10^3)$ Pa has been obtained from core surface velocity models, assuming a local balance of force (tangential geostrophy) at the core surface (Jault & Le Mouél 1990). These models have now been superseded by quasi-geostrophic (QG) models that rely on a global assumption, for which it is assumed that the equatorial components of the fluid velocity are invariant along the rotation axis, as observed at leading order in numerical simulations (e.g. Gillet et al. 2011; Schaeffer et al. 2017). QG models have been shown to capture the fundamental features of rapidly rotating hydrodynamics by comparing with three-

dimensional (3-D) numerical simulations (Guervilly et al. 2019; Gastine 2019). Furthermore, QG models incorporating the magnetic field have been used to investigate spherical TM (Canet et al. 2014; Labbé et al. 2015). In this framework, the surface pressure cannot be inferred from the velocity. In the most general case, the pressure is a 3-D quantity given by the Lagrange multiplier associated to incompressibility. For QG models we can introduce a Lagrange multiplier associated to incompressibility, but it is only a two-dimensional (2-D) function of the coordinates in the equatorial plane. Therefore, we cannot infer the 3-D pressure at the CMB from the velocity field only.

For an axisymmetric core, the axial pressure torque vanishes exactly for any flow. To investigate the influence of non-axisymmetric CMBs, the ellipsoidal geometry can be considered as a first step. From seismological observations a peak-to-peak amplitude of CMB topography of about 3 km has been inferred (Sze & van der Hilst 2003; Koper et al. 2003), corresponding to an equatorial ellipticity $\mathcal{O}(10^{-3})$.

Here, we derive a generic QG model that does not assume axisymmetry, which is then compared to a hybrid model using QG velocities and 3-D magnetic fields in the case of an ellipsoid. We present the linear modes and their axial angular momentum, as well as the hydrodynamic pressure torque that the fluid exerts on the solid container. Lastly, we discuss the possible implications of this study for Earth-like liquid cores.

2 PROBLEM SETUP

2.1 Magnetohydrodynamic equations

We consider a fluid of homogeneous density ρ , uniform kinematic viscosity ν and magnetic diffusivity η , which is enclosed in a rigid container of volume \mathcal{V} and boundary $\partial\mathcal{V}$. The time evolution of the velocity field \mathbf{u} and the magnetic field \mathbf{B} is given by the incompressible magnetohydrodynamics (MHD) equations. In the reference frame rotating with the angular velocity $\boldsymbol{\Omega}$, they read

$$\frac{\partial \mathbf{u}}{\partial t} + (\mathbf{u} \cdot \nabla) \mathbf{u} = -2\boldsymbol{\Omega} \times \mathbf{u} - \frac{1}{\rho} \nabla p + \nu \nabla^2 \mathbf{u} + \frac{1}{\mu_0 \rho} (\nabla \times \mathbf{B}) \times \mathbf{B}, \quad (1a)$$

$$\frac{\partial \mathbf{B}}{\partial t} = \nabla \times (\mathbf{u} \times \mathbf{B}) + \eta \nabla^2 \mathbf{B}, \quad (1b)$$

with p the reduced pressure and μ_0 the magnetic permeability in vacuum. MHD equations (1) are completed by the solenoidal conditions $\nabla \cdot \mathbf{B} = \nabla \cdot \mathbf{u} = 0$. The characteristic length scale R_0 is determined by the container size, which is taken as its mean radius. In ellipsoids, R_0 is the geometric mean $R_0 = (abc)^{1/3}$ of the three semi-major axes $[a, b, c]$. The angular velocity is given by $\boldsymbol{\Omega} = \Omega \mathbf{1}_\Omega$ and the characteristic background magnetic field strength is B_0 . We define the characteristic time $t_0 = R_0/u_A$, where $u_A = B_0/\sqrt{\rho\mu_0}$ is the characteristic Alfvén wave velocity. The characteristic pressure is then given by ρu_A^2 . The dimensionless equations

read

$$\frac{\partial \mathbf{u}}{\partial t} + (\mathbf{u} \cdot \nabla) \mathbf{u} = -\frac{2}{\text{Le}} \mathbf{1}_\Omega \times \mathbf{u} - \nabla p + \frac{\text{Pm}}{\text{Lu}} \nabla^2 \mathbf{u} + (\nabla \times \mathbf{B}) \times \mathbf{B}, \quad (2a)$$

$$\frac{\partial \mathbf{B}}{\partial t} = \nabla \times (\mathbf{u} \times \mathbf{B}) + \frac{1}{\text{Lu}} \nabla^2 \mathbf{B}, \quad (2b)$$

where we introduce the Lehnert number Le (measuring the strength of the Lorentz force relative to the Coriolis force), the Lundquist number Lu (comparing magnetic induction to magnetic diffusion), and the magnetic Prandtl number Pm (comparing kinematic viscosity to magnetic diffusion). They are given by

$$\text{Le} = \frac{B_0}{\Omega R_0 \sqrt{\mu_0 \rho}}, \quad \text{Lu} = \frac{R_0 B_0}{\eta \sqrt{\mu_0 \rho}}, \quad \text{Pm} = \frac{\nu}{\eta}. \quad (3)$$

Typical values for the Earth's outer core, with radius $R_0 \approx 3478$ km, kinematic viscosity $\nu \approx 10^{-6}$ m²s⁻¹ (Wijs et al. 1998), mean radial magnetic field strength $B_0 \approx 3$ mT (Gillet et al. 2010) and electrical conductivity $\sigma \approx 1.55 \times 10^6$ Sm⁻¹ (Pozzo et al. 2014), are $\text{Le} = \mathcal{O}(10^{-4})$, $\text{Lu} = \mathcal{O}(10^5)$ and $\text{Pm} = \mathcal{O}(10^{-6})$. The dynamics we will be considering operate on timescales shorter than magnetic diffusion and viscous spin-up times. Hence, we will neglect viscous and Ohmic dissipations. The governing equations are

$$\frac{\partial \mathbf{u}}{\partial t} + (\mathbf{u} \cdot \nabla) \mathbf{u} = -\frac{2}{\text{Le}} \mathbf{1}_\Omega \times \mathbf{u} - \nabla p + (\nabla \times \mathbf{B}) \times \mathbf{B}, \quad (4a)$$

$$\frac{\partial \mathbf{B}}{\partial t} = \nabla \times (\mathbf{u} \times \mathbf{B}). \quad (4b)$$

Equations (4) are supplemented with appropriate boundary conditions. In the diffusionless approximation, the velocity needs to satisfy only the non-penetration condition $\mathbf{u} \cdot \mathbf{n} = 0$ on ∂V . If $\mathbf{B} \cdot \mathbf{n} = 0$ at an initial time $t = 0$, the normal component of the induction equation ensures that the normal component of \mathbf{B} is zero at all later times (see Backus et al. 1996).

2.2 Torque balance

The net torque balance of the system is given by

$$\frac{\partial \mathbf{L}}{\partial t} + \boldsymbol{\Gamma}_c = \boldsymbol{\Gamma}_p + \boldsymbol{\Gamma}_L, \quad (5)$$

with the angular momentum \mathbf{L} , the hydrodynamic pressure torque $\boldsymbol{\Gamma}_p$, the Coriolis torque $\boldsymbol{\Gamma}_c$ and the Lorentz torque $\boldsymbol{\Gamma}_L$ given by

$$\mathbf{L} = \int_{\mathcal{V}} \mathbf{r} \times \mathbf{u} dV, \quad (6a)$$

$$\boldsymbol{\Gamma}_p = - \int_{\mathcal{V}} \mathbf{r} \times \nabla p dV = - \int_{\partial V} p (\mathbf{r} \times \mathbf{n}) dS, \quad (6b)$$

$$\boldsymbol{\Gamma}_c = 2 \int_{\mathcal{V}} \mathbf{r} \times (\boldsymbol{\Omega} \times \mathbf{u}) dV, \quad (6c)$$

$$\boldsymbol{\Gamma}_L = \int_{\mathcal{V}} \mathbf{r} \times ((\nabla \times \mathbf{B}) \times \mathbf{B}) dV. \quad (6d)$$

We can further split up the Lorentz torque into magnetic pressure torque $\boldsymbol{\Gamma}_{\text{pm}}$ and a magnetic tension torque $\boldsymbol{\Gamma}_b$ as

$$\boldsymbol{\Gamma}_L = \boldsymbol{\Gamma}_b + \boldsymbol{\Gamma}_{\text{pm}}, \quad (7)$$

with

$$\mathbf{\Gamma}_{\text{pm}} = -\frac{1}{2} \int_{\mathcal{V}} \mathbf{r} \times \nabla (\mathbf{B}^2) dV = -\frac{1}{2} \int_{\partial\mathcal{V}} \mathbf{B}^2 (\mathbf{r} \times \mathbf{n}) dS, \quad (8a)$$

$$\mathbf{\Gamma}_{\text{b}} = \int_{\mathcal{V}} \mathbf{r} \times ((\mathbf{B} \cdot \nabla) \mathbf{B}) dV. \quad (8b)$$

For a perfectly conducting boundary (with $\mathbf{B} \cdot \mathbf{n} = 0$ on $\partial\mathcal{V}$), $\mathbf{\Gamma}_{\text{b}}$ vanishes exactly (see equation 45 in Roberts & Auromou 2012) and only the magnetic pressure torque $\mathbf{\Gamma}_{\text{pm}}$ contributes to the torque balance (5).

The axial component of the Coriolis torque $\mathbf{\Gamma}_{\text{c}}$ also vanishes (see equation 14.98 in Davidson 2016). In the axial direction, the torque balance reduces to

$$\frac{\partial L_z}{\partial t} = \Gamma_{\text{p},z} + \Gamma_{\text{pm},z}. \quad (9)$$

Hence, any changes of the axial angular momentum of the fluid can only result from the unbalance between the magnetic and hydrodynamic pressure torques. For the sphere, the transformation of the volume integral into a surface integral shows that the pressure torques (6b) and (8a) vanish, so that no change in angular momentum is possible.

2.3 Geostrophic motions and torsional Alfvén modes

In a container of volume \mathcal{V} that can be continuously deformed into a sphere, such that the height of the fluid column h along the rotation axis is a homeomorphism between the volume \mathcal{V} and the sphere, all contours of constant h (geostrophic contours) are closed. Examples of such containers include the full sphere (not a spherical shell) or ellipsoids. It is often postulated that incompressible flows in such a container can be expanded as (e.g. Greenspan 1968)

$$\mathbf{u} = \sum_j \gamma_j(t) \mathbf{u}_{G,j}(\mathbf{r}_{\perp}) + \sum_i \alpha_i(t) \mathbf{u}_i(\mathbf{r}), \quad (10)$$

where $\mathbf{u}_{G,j}(\mathbf{r}_{\perp})$ are the (degenerate) geostrophic solutions (e.g. Liao & Zhang 2010, in spheres) that only depend on the position perpendicular to the rotation axis \mathbf{r}_{\perp} . They are given by the geostrophic equilibrium

$$2\mathbf{\Omega} \times \mathbf{u}_{G,j} = -\nabla p_{G,j}, \quad (11)$$

and their superposition is commonly referred to as the geostrophic mode $\mathbf{u}_G = \sum_j \mathbf{u}_{G,j}$ (e.g. Greenspan 1968). Additionally, $\mathbf{u}_i(\mathbf{r})$ are the spatial eigensolutions of the inertial wave equation (e.g. Vantighem 2014, in ellipsoids)

$$\frac{\partial \mathbf{u}_i}{\partial t} + 2\mathbf{\Omega} \times \mathbf{u}_i = -\nabla p_i. \quad (12)$$

Expansion (10) has proven to be exact for the ellipsoid (Backus & Rieutord 2017; Ivers 2017).

From balance (11) it is clear that the axial geostrophic pressure torque vanishes, as the axial Coriolis torque vanishes for any flow \mathbf{u} . However, this is no longer the case when the flow is time dependent, even if it remains mainly geostrophic (or 'pseudo-geostrophic', Gans 1971), such that $\mathbf{u}_{PG}(\mathbf{r}_{\perp}, t) \simeq \sum_j \gamma_j(t) \mathbf{u}_{G,j}$ (i.e. with $|\gamma_j| \gg |\alpha_i|$). In the presence of a Lorentz force the pseudo-geostrophic flow is governed by

$$\frac{\partial \mathbf{u}_{PG}}{\partial t} = -\frac{2}{\text{Le}} \mathbf{1}_{\Omega} \times \mathbf{u}_{PG} - \nabla p + (\nabla \times \mathbf{B}) \times \mathbf{B}. \quad (13)$$

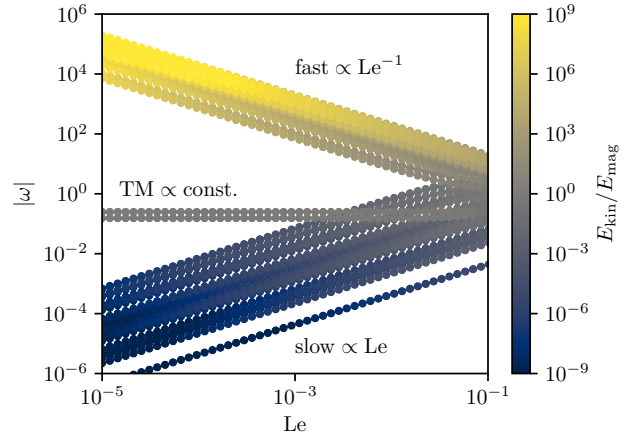


Figure 1. Mode frequencies as a function of Lehnert number in the sphere. The imposed magnetic field is $\mathbf{B}_0 = (-y, x - z/10, x/10)^T$, following Vidal et al. (2019). The colours indicate the ratio of kinetic energy to magnetic energy, where yellow indicates a larger kinetic energy and blue a larger magnetic energy. The modes are separated into slow modes, fast modes and TM for $\text{Le} \ll 1$.

Using the geostrophic equilibrium (11) we substitute the Coriolis acceleration for its pressure gradient. Additionally, rewriting the Lorentz force in terms of the magnetic pressure gradient and the Maxwell term, (13) takes the form

$$\frac{\partial \mathbf{u}_{PG}}{\partial t} = -\nabla(p_A + p_m) + (\mathbf{B} \cdot \nabla) \mathbf{B}, \quad (14)$$

with $p_A = p - \sum_j \gamma_j p_{G,j}$ and $p_m = \mathbf{B}^2/2$. Besides the magnetic pressure p_m , an ageostrophic component p_A remains in the pressure. They may both exert a torque on the container if it is not spherical.

TM, also called 'torsional oscillations' (Braginsky 1970), are examples of such pseudo-geostrophic flows. They are solutions of the linearised equations (4) for $\text{Le} \ll 1$, and reduce to the ordinary geostrophic mode in the limit $\text{Le} \rightarrow 0$. When scaled by the reciprocal of the Alfvén time scale T_A , the TM frequencies are constant (see Figure 1). Their Alfvén wave nature is also evident in the ratio of kinetic energy to magnetic energy, which is $\mathcal{O}(1)$ as indicated by the grey colour in Figure 1. We define TM to have a frequency independent of Le when $\text{Le} \ll 1$ (if scaled by T_A^{-1}) and of approximately unit ratio between kinetic and magnetic energy. These two features clearly differentiate them from other modes present, namely the so-called fast modes and slow modes. The fast modes are slightly modified inertial modes, with frequencies on the order of the angular frequency, and their energy is mostly kinetic (see Figure 1, yellow dots). The slow modes (or Magneto-Coriolis modes) have a frequency much lower than the angular frequency and a small kinetic energy compared to the magnetic energy (see Figure 1, dark blue dots).

In the axisymmetric case, the geostrophic mode can be written as $\mathbf{u}_G = u_G(s) \mathbf{1}_{\phi}$ and a pseudo-geostrophic flow is simply $\mathbf{u}_{PG} \simeq u_{PG}(s, t) \mathbf{1}_{\phi}$ (with s the cylindrical radius and ϕ the azimuthal angle). The projection of the linearised momentum equation (4a) onto the geostrophic mode reduces

to the one-dimensional equation

$$\rho h \frac{\partial^2 u_{PG}(s, t)}{\partial t^2} = \frac{1}{s^2} \frac{\partial}{\partial s} \left(h s^3 \frac{\partial}{\partial s} \left(\frac{u_{PG}(s, t)}{s} \right) \int B_s^2 dz \right), \quad (15)$$

only depending on the radial distance s to the rotation axis. Roberts & Aurnou (2012) referred to this equation as the canonical torsional wave equation. We refer the reader to Roberts (1972) and Jault (2003) for details on the derivation. In the case of the ellipsoid, we shall consider TM within the framework of a QG model retaining ageostrophic components of the flow.

2.4 Quasi-geostrophic equation with generic geostrophic contours

We assume that the horizontal velocity components are independent of the coordinate z along the rotation axis, $\mathbf{u}_\perp = \mathbf{u}_\perp(\mathbf{r}_\perp, t)$. Together with the non-penetration boundary condition, $\mathbf{u} \cdot \mathbf{n} = 0$ on $\partial\mathcal{V}$, the mass continuity equation $\nabla \cdot \mathbf{u} = 0$ and the assumption of an equatorially symmetric volume \mathcal{V} the QG velocity takes the form (e.g. Bardsley 2018)

$$\mathbf{u} = \mathbf{u}_\perp(\mathbf{r}_\perp, t) + u_z \mathbf{1}_z = \nabla \psi \times \nabla \left(\frac{z}{h} \right), \quad (16)$$

with $h = h(\mathbf{r}_\perp)$ the height of the fluid column, $\mathbf{u}_\perp(\mathbf{r}_\perp, t) = \frac{1}{h} \nabla \psi \times \mathbf{1}_z$, $u_z = \frac{z}{h} \mathbf{u}_\perp \cdot \nabla h$ and $\psi = \psi(\mathbf{r}_\perp, t)$ a scalar stream function. By construction, ψ is constant at the equator $\partial\mathcal{A}$ for the volume \mathcal{V} considered here. Following the boundary condition arising naturally when $h \rightarrow 0$ at $\partial\mathcal{A}$ (Maffei et al. 2017), we choose $\psi = 0$ on $\partial\mathcal{A}$. Note that, if ψ is constant along geostrophic contours (i.e. it is a function of h only), we recover the geostrophic velocity (see Appendix A).

To derive an evolution equation for this scalar stream function, we project the momentum equation (4a) onto the subset \mathbf{u}' of QG velocities (16) following Labbé et al. (2015) and Bardsley (2018). This method is essentially a variational approach, which consists in finding solutions \mathbf{u} satisfying

$$\int_{\mathcal{V}} \mathbf{u}' \cdot \mathbf{f}(\mathbf{u}) dV = 0, \quad \forall \mathbf{u}' \quad (17)$$

where

$$\mathbf{f}(\mathbf{u}) = \frac{\partial \mathbf{u}}{\partial t} + (\mathbf{u} \cdot \nabla) \mathbf{u} + \frac{2}{Le} \mathbf{1}_\Omega \times \mathbf{u} + \nabla p - (\nabla \times \mathbf{B}) \times \mathbf{B}, \quad (18)$$

with \mathbf{u}' and \mathbf{u} of the form (16). Substituting (16) into (17) yields

$$\int_{\mathcal{V}} \mathbf{u}' \cdot \mathbf{f} dV = \int_{\mathcal{V}} \nabla \psi' \times \nabla \left(\frac{z}{h} \right) \cdot \mathbf{f} dV, \quad (19a)$$

$$= \int_{\mathcal{A}} \nabla \psi' \cdot \left\langle \nabla \left(\frac{z}{h} \right) \times \mathbf{f} \right\rangle dS, \quad (19b)$$

$$= - \int_{\mathcal{A}} \psi' \nabla \cdot \left\langle \nabla \left(\frac{z}{h} \right) \times \mathbf{f} \right\rangle dS, \quad (19c)$$

$$= - \int_{\mathcal{A}} \psi' \mathcal{Q}(\mathbf{f}) dS, \quad (19d)$$

with the projection operator \mathcal{Q} defined as

$$\mathcal{Q}(\mathbf{f}) = \nabla \cdot \left\langle \nabla \left(\frac{z}{h} \right) \times \mathbf{f} \right\rangle, \quad (20)$$

where $\langle \cdot \rangle = \int_{-h}^h \cdot dz$ is the integral along the rotation axis

and $\int_{\mathcal{A}} \cdot dS$ the integral over the equatorial surface plane \mathcal{A} (shown in Figure 2 for the ellipsoid). In this step, we made use of the boundary condition $\psi = 0$ at the equator $\partial\mathcal{A}$. For expression (19d) to be zero for any test function ψ' , the QG velocity \mathbf{u} must satisfy

$$\mathcal{Q} \left(\frac{\partial \mathbf{u}}{\partial t} + \mathbf{u} \cdot \nabla \mathbf{u} + \frac{2}{Le} \mathbf{1}_\Omega \times \mathbf{u} - (\nabla \times \mathbf{B}) \times \mathbf{B} \right) = 0, \quad (21)$$

where the pressure gradient is omitted, as it vanishes in the projection.

First, we consider the inertial term, which simplifies as

$$\mathcal{Q} \left(\frac{\partial \mathbf{u}}{\partial t} \right) = \nabla \cdot \left\langle \nabla \left(\frac{z}{h} \right) \times \left(\nabla \frac{\partial \psi}{\partial t} \times \nabla \left(\frac{z}{h} \right) \right) \right\rangle, \quad (22a)$$

$$= 2\mathcal{D} \frac{\partial \psi}{\partial t}, \quad (22b)$$

with

$$\mathcal{D}\Psi = \nabla \cdot \left(\frac{1}{h} \nabla \Psi + \frac{1}{3h} \nabla h \times (\nabla \Psi \times \nabla h) \right). \quad (23)$$

We can derive the projection for a force in the form of $\boldsymbol{\xi} \times \mathbf{u}$ as follows

$$\mathcal{Q}(\boldsymbol{\xi} \times \mathbf{u}) = \nabla \cdot \left\langle - \left(\nabla \left(\frac{z}{h} \right) \cdot \boldsymbol{\xi} \right) \mathbf{u} \right\rangle, \quad (24)$$

which holds for any \mathbf{u} satisfying the boundary condition $\mathbf{u} \cdot \mathbf{n} = 0$ on $\partial\mathcal{V}$. We may further simplify this by considering $\Phi = -\nabla \left(\frac{z}{h} \right) \cdot \boldsymbol{\xi}$

$$\nabla \cdot \langle \Phi \mathbf{u} \rangle = \nabla \cdot \left\langle \frac{\Phi}{h} \nabla \times \mathbf{1}_z + \Phi z \nabla \psi \times \nabla \left(\frac{1}{h} \right) \right\rangle, \quad (25a)$$

$$= \nabla \cdot \left\langle \frac{\langle \Phi \rangle}{h} \nabla \psi \times \mathbf{1}_z + \langle z \Phi \rangle \nabla \psi \times \nabla \left(\frac{1}{h} \right) \right\rangle, \quad (25b)$$

$$= \left\{ \frac{\langle \Phi \rangle}{h}, \psi \right\}, \quad (25c)$$

with

$$\{X, Y\} = (\nabla X \times \nabla Y) \cdot \mathbf{1}_z. \quad (26)$$

Let us write $\mathbf{u} \cdot \nabla \mathbf{u} = (\nabla \times \mathbf{u}) \times \mathbf{u} + \nabla \mathbf{u}^2/2$. Since the gradient term vanishes exactly in the projection, the non-linear term can be written in the generic form $\boldsymbol{\xi} \times \mathbf{u}$, with $\boldsymbol{\xi} = \nabla \times \mathbf{u}$. For the non-linear term we thus have

$$\langle \Phi \rangle = \left\langle -\nabla \left(\frac{z}{h} \right) \cdot (\nabla \times \mathbf{u}) \right\rangle, \quad (27a)$$

$$= \left\langle \nabla \cdot \left(\nabla \left(\frac{z}{h} \right) \times \left(\nabla \psi \times \nabla \left(\frac{z}{h} \right) \right) \right) \right\rangle, \quad (27b)$$

$$= 2\mathcal{D}\psi. \quad (27c)$$

We have used here $\langle \nabla \cdot \mathbf{x} \rangle = \nabla \cdot \langle \mathbf{x} \rangle$, which can be demonstrated to hold for $\mathbf{x} = \nabla \left(\frac{z}{h} \right) \times \left(\nabla \psi \times \nabla \left(\frac{z}{h} \right) \right)$. The non-linear term is then given by

$$\mathcal{Q}((\nabla \times \mathbf{u}) \times \mathbf{u}) = 2 \left\{ \frac{1}{h} \mathcal{D}\psi, \psi \right\}. \quad (28)$$

For the Coriolis force $\boldsymbol{\xi} = 2/Le \mathbf{1}_\Omega$ and thus $\langle \Phi \rangle = \langle -\nabla \left(\frac{z}{h} \right) \cdot \boldsymbol{\Omega} \rangle = -4/Le$, so that the Coriolis force reduces to

$$\mathcal{Q} \left(\frac{2}{Le} \mathbf{1}_\Omega \times \mathbf{u} \right) = -\frac{4}{Le} \left\{ \frac{1}{h}, \psi \right\}. \quad (29)$$

The QG scalar momentum equation is then given by

$$\mathcal{D} \frac{\partial \psi}{\partial t} + \left\{ \frac{1}{h} \mathcal{D} \psi, \psi \right\} = \frac{2}{\text{Le}} \left\{ \frac{1}{h}, \psi \right\} + \frac{1}{2} \mathcal{Q}((\nabla \times \mathbf{B}) \times \mathbf{B}). \quad (30)$$

We can close the system by assuming that the 3-D magnetic field in (30) is advected only by the QG velocity. This is, to the authors' knowledge, the first presentation of a hybrid model with QG velocities and 3-D magnetic field. Such a model is desirable especially in geodynamo modelling, where it is found that a strong columnar motion is accompanied by a magnetic field of 3-D structure (e.g. Schaeffer et al. 2017).

To derive a fully 2D model we assume the same form for the magnetic field, as for the velocity

$$\mathbf{B} = \nabla A \times \nabla \left(\frac{z}{h} \right), \quad (31)$$

with $A = A(\mathbf{r}_\perp, t)$ a scalar potential. By construction, such a magnetic field satisfies the perfectly conducting boundary condition $\mathbf{B} \cdot \mathbf{n} = 0$. This approximation has been used previously to investigate TM in QG models (Canet et al. 2014; Labbé et al. 2015). Under this assumption, the Lorentz term simplifies analogous to (28), such that

$$\mathcal{Q}((\nabla \times \mathbf{B}) \times \mathbf{B}) = 2 \left\{ \frac{1}{h} \mathcal{D} A, A \right\}. \quad (32)$$

The scalar momentum equation is then written in terms of ψ and A only

$$\mathcal{D} \frac{\partial \psi}{\partial t} + \left\{ \frac{1}{h} \mathcal{D} \psi, \psi \right\} = 2\Omega \left\{ \frac{1}{h}, \psi \right\} + \left\{ \frac{1}{h} \mathcal{D} A, A \right\}. \quad (33)$$

The ideal induction equation (4b) can be simplified as follows

$$\mathbf{u} \times \mathbf{B} = \frac{1}{h^2} \nabla \psi \times \nabla A - \frac{z}{h^3} \{ \psi, A \} \nabla h, \quad (34)$$

$$= \frac{C}{h} \mathbf{1}_z - \frac{Cz}{h^2} \nabla h, \quad (35)$$

with $C = \frac{1}{h} \{ \psi, A \}$. Taking the curl then gives

$$\nabla \times (\mathbf{u} \times \mathbf{B}) = \frac{1}{h} \nabla C \times \mathbf{1}_z - \frac{z}{h^2} \nabla C \times \nabla h \quad (36a)$$

$$= \nabla C \times \nabla \left(\frac{z}{h} \right). \quad (36b)$$

Thus, the induction equation is given by

$$\frac{\partial A}{\partial t} = \frac{1}{h} \{ \psi, A \}. \quad (37)$$

In the sphere, where cylindrical coordinates apply, the equations (33) and (37) are exactly equivalent to the equations obtained by Labbé et al. (2015).

3 METHODS FOR THE ELLIPSOID

We now consider the case of an ellipsoid with semi axes a , b and c defined by

$$\frac{x^2}{a^2} + \frac{y^2}{b^2} + \frac{z^2}{c^2} = 1. \quad (38)$$

To keep equatorial symmetry, we also consider that the rotation axis is aligned with the c -axis, $\mathbf{1}_\Omega = \mathbf{1}_z$ (Figure 2).

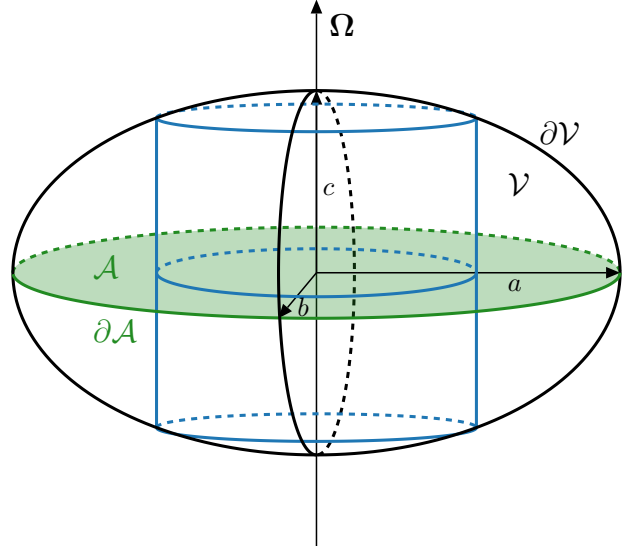


Figure 2. Schematic of a geostrophic column (blue) in an ellipsoid of volume \mathcal{V} where one of the principal axes is aligned with the rotation axis Ω . The area of the equatorial plane \mathcal{A} is shaded in green.

3.1 Cartesian monomial basis in the ellipsoid

Since the ellipsoid is a quadratic surface, smooth-enough solutions can be sought by using an infinite sequence of Cartesian polynomials (Lebovitz 1989). This approach has proven accurate to describe 3-D inviscid flows in ellipsoids (e.g. Vantighem et al. 2015; Vidal & Cébron 2017; Vidal et al. 2020). The 3-D inertial modes are exactly described by polynomials in the ellipsoid (Backus & Rieutord 2017; Ivers 2017), and also the QG and 3-D inertial modes in the spheroid (Maffei et al. 2017; Zhang & Liao 2017). Additionally, the MHD modes upon idealised background magnetic fields (e.g. Malkus 1967) also have an exact polynomial description in the spheroid (Kerswell 1994) and the ellipsoid (Vidal et al. 2016).

Similarly, a 2-D polynomial decomposition in the Cartesian coordinates can be obtained for arbitrary QG vector (16) in non-axisymmetric ellipsoids as follows. To satisfy the polynomial form of the velocity components, the stream function must be given as

$$\psi = h^3 \Pi(x, y) = h^3 \sum_i \hat{\alpha}_i \Pi_i, \quad (39)$$

with the complex-valued coefficients $\hat{\alpha}_i$ and the monomials

$$\Pi_i = 1, x, y, xy, x^2, \dots, x^{N-1}, y^{N-1} \quad (40)$$

with $i \in [0, N_2]$ and $N_2 = N(N+1)/2$. At any point (x, y) we have

$$\frac{h^2}{c^2} = 1 - \frac{x^2}{a^2} - \frac{y^2}{b^2}. \quad (41)$$

If additionally we define $G = h^2/2$, we can rewrite

$$h \nabla h = \nabla G. \quad (42)$$

Then, the QG basis vectors \mathbf{u}_i are given by

$$\mathbf{u}_i = h^2 \nabla \Pi_i \times \mathbf{1}_z + 3 \Pi_i \nabla G \times \mathbf{1}_z - z \nabla \Pi_i \times \nabla G, \quad (43)$$

with the first three basis elements

$$\mathbf{u}_0 = 3c^2 \begin{pmatrix} -y/b^2 \\ x/a^2 \\ 0 \end{pmatrix}, \quad (44a)$$

$$\mathbf{u}_1 = c^2 \begin{pmatrix} 1 - x^2/a^2 - 4y^2/b^2 \\ 3xy/a^2 \\ -xz/a^2 \end{pmatrix}, \quad (44b)$$

$$\mathbf{u}_2 = c^2 \begin{pmatrix} -3xy/b^2 \\ 4x^2/a^2 + y^2/b^2 - 1 \\ yz/b^2 \end{pmatrix}. \quad (44c)$$

The full velocity is reconstructed by

$$\mathbf{u} = \sum_{i=0}^{N_2} \hat{\alpha}_i \mathbf{u}_i. \quad (45)$$

For the linear hydrodynamic (Rossby wave) problem

$$\mathcal{D} \frac{\partial \psi}{\partial t} = 2\Omega \left\{ \frac{1}{h}, \psi \right\}, \quad (46)$$

the polynomial degree of $\psi_i = \hat{\alpha}_i h^3 \Pi_i$ is preserved, that is the QG inertia and Coriolis operators do not modify (increase) the polynomial degree, similar to the 3-D Coriolis operator in the ellipsoid (Backus & Rieutord 2017; Ivers 2017). This is no longer the case in the presence of a background magnetic field within the QG model (unless the magnetic field is only linear in the spatial coordinates, see Malkus 1967), as the Lorentz term modifies the polynomial degree. Then, the exact solutions cannot be obtained from a finite set of Π_i . Hence, we must project the governing equations onto the basis with a sufficiently large maximum polynomial degree.

3.2 Galerkin method

Since we are interested in the wave properties, we linearise equations (4) around a background state with no motion and steady magnetic field \mathbf{B}_0 . In the Earth's core, the characteristic mean velocity field is thought to be negligible compared to the Alfvén wave velocity (Gillet et al. 2015; Brenzung et al. 2018). Hence, the velocity and magnetic perturbations $[\tilde{\mathbf{u}}, \tilde{\mathbf{B}}]$ are given by

$$\frac{\partial \tilde{\mathbf{u}}}{\partial t} + \frac{2}{\text{Le}} \mathbf{1}_\Omega \times \tilde{\mathbf{u}} = -\nabla p + (\nabla \times \mathbf{B}_0) \times \tilde{\mathbf{B}} + (\nabla \times \tilde{\mathbf{B}}) \times \mathbf{B}_0, \quad (47a)$$

$$\frac{\partial \tilde{\mathbf{B}}}{\partial t} = \nabla \times (\tilde{\mathbf{u}} \times \mathbf{B}_0). \quad (47b)$$

The linearised set of equations in the hybrid model then read

$$\mathcal{D} \frac{\partial \tilde{\psi}}{\partial t} = \frac{2}{\text{Le}} \left\{ \frac{1}{h}, \tilde{\psi} \right\} + \frac{1}{2} \mathcal{Q}((\nabla \times \mathbf{B}_0) \times \tilde{\mathbf{B}} + \frac{1}{2} \mathcal{Q}((\nabla \times \tilde{\mathbf{B}}) \times \mathbf{B}_0), \quad (48a)$$

$$\frac{\partial \tilde{\mathbf{B}}}{\partial t} = \nabla \times \left((\nabla \tilde{\psi} \times \nabla \left(\frac{z}{h} \right)) \times \mathbf{B}_0 \right). \quad (48b)$$

The linearisation of the magnetic field translates to $A = A_0 + \tilde{A}$ for the scalar potential and the scalar QG equations

(33) and (37) read

$$\partial_t \mathcal{D} \tilde{\psi} - \frac{2}{\text{Le}} \left\{ \frac{1}{h}, \tilde{\psi} \right\} = \left\{ \frac{1}{h} \mathcal{D} \tilde{A}, A_0 \right\} + \left\{ \frac{1}{h} \mathcal{D} A_0, \tilde{A} \right\}, \quad (49a)$$

$$\frac{\partial \tilde{A}}{\partial t} = \frac{1}{h} \{ \tilde{\psi}, A_0 \}. \quad (49b)$$

To solve such sets of linearised equations for eigenmodes, Fourier expansions along the azimuthal direction could be used in the sphere, combined with finite differences in the radial direction (Labbé et al. 2015). Here, we use a Galerkin approach to project the governing equations onto the respective polynomial bases (e.g. Vidal & Cébron 2017; Vidal et al. 2020). This approach is suitable for the Cartesian monomial basis, as we can analytically integrate the Cartesian monomials occurring in the inner product (see formula 50 in Lebovitz 1989). For the QG model this projection is given by

$$f_{ij} = \int_{\mathcal{A}} \tilde{\psi}_i f(\tilde{\psi}_j, \tilde{A}_j) dS, \quad (50)$$

where now $f(\tilde{\psi}, \tilde{A})$ corresponds to a force in the scalar momentum equation (49a). In this way we create coefficient matrices U_{ij} , C_{ij} and L_{ij} for the inertial, Coriolis and Lorentz force, respectively. Analogously, the induction equation (49b) is projected onto the basis $A_i = \hat{\zeta}_i h^3 \Pi_i$ and the coefficient matrices B_{ij} and V_{ij} correspond to the projections of the temporal change of the magnetic field and magnetic advection, respectively. For this model U_{ij} and B_{ij} are identical and Hermitian. Assuming that $\tilde{\psi}(\mathbf{r}_\perp, t) = \hat{\psi}(\mathbf{r}_\perp) \exp(i\omega t)$ (and the same for \tilde{A}), so that $\partial_t \tilde{\psi} = i\omega \tilde{\psi}$, the resulting matrix form is

$$i\omega \mathbf{M} \mathbf{x} = \mathbf{D} \mathbf{x}, \quad (51)$$

with $\mathbf{M}, \mathbf{D} \in \mathbb{R}^{2N_2 \times 2N_2}$ of the form

$$\mathbf{M} = \begin{pmatrix} U_{ij} & 0 \\ 0 & B_{ij} \end{pmatrix}, \quad \mathbf{D} = \begin{pmatrix} C_{ij} & L_{ij} \\ V_{ij} & 0 \end{pmatrix}, \quad (52)$$

and $\mathbf{x} = (\hat{\alpha}_j, \hat{\zeta}_j) \in \mathbb{C}^{2N_2}$. This form is referred to as a generalised eigen problem solvable for eigen pairs (ω_k, \mathbf{x}_k) .

Note that using the reduced equation and projecting onto the basis of stream functions ψ_i is equivalent to projecting the 3-D equations onto the QG basis \mathbf{u}_i , apparent from (19). We use this fact for the hybrid model and project the 3-D momentum equation (47a) onto the QG basis vectors \mathbf{u}_i while keeping the full 3-D basis vectors \mathbf{B}_i with coefficients ζ_i for the magnetic field. The induction equation (47b) is projected onto the basis \mathbf{B}_i . The resulting matrices are $U'_{ij}, C'_{ij} \in \mathbb{R}^{N_2 \times N_2}$, $L'_{ij} \in \mathbb{R}^{N_2 \times N_3}$, $B_{ij} \in \mathbb{R}^{N_3 \times N_3}$ and $V'_{ij} \in \mathbb{R}^{N_3 \times N_2}$, so that $\mathbf{M}', \mathbf{D}' \in \mathbb{R}^{N_2+N_3 \times N_2+N_3}$ and $\mathbf{x} = (\hat{\alpha}_j, \zeta_j) \in \mathbb{C}^{N_2+N_3}$. These matrices can be built analytically, but this becomes tedious even for a maximum polynomial degree as low as 2 and in practise this is done by computer algebra systems or numerically.

3.3 Numerical implementation

The linear problems based on Cartesian monomials are implemented in the Julia programming language (Bezanson et al. 2017). The QG, hybrid and 3-D models are freely available at <https://github.com/fgerick/Mire.jl>. The reproduction of all the results and figures from this article using

these models is available through <https://dx.doi.org/10.5281/zenodo.3631244>.

To solve for the eigen problems, different methods have been employed. To calculate the full spectrum of eigensolutions, we use either LAPACK or recent Julia implementations for accuracy beyond standard floating point numbers (e.g. in Figure 9 below). Full spectrum eigensolutions are computationally demanding, which is why we also apply targeted iterative solvers from the ARPACK library, making use of the sparsity of the matrices \mathbf{M} and \mathbf{D} , where approximately 13% and 30% of entries are non-zero, respectively. The sparse solver is also applied to follow eigenbranches (i.e. to track a specific eigensolution through the parameter space). To do so, we apply a targeted shift-and-invert method (e.g. Rieutord & Valdettaro 1997; Vidal & Schaeffer 2015)

$$(\mathbf{D} - \sigma\mathbf{M})^{-1}\mathbf{D}\mathbf{x} = \lambda\mathbf{x} \quad (53)$$

around a target $\sigma \in \mathbb{C}$, with the new eigenvalue $\lambda = (i\omega - \sigma)^{-1}$. This strategy is efficient to compute the eigenvalues close to the target σ (which is chosen close to the desired eigenvalue $i\omega$).

4 NUMERICAL RESULTS

We first validate our QG (and hybrid) model against the 3-D model for a simplified background magnetic field (Malkus 1967), and then consider a more complex background magnetic field that is able to drive TM. In this section the QG model is considered and we compare our results to a 3-D magnetic field with the hybrid model in Appendix B.

4.1 Modes in the Malkus field

An interesting first study case is the mean field introduced by Malkus (1967), originally given as a field of uniform current along the rotation axis in a sphere with $\mathbf{B}_{0,M} = s\mathbf{1}_\phi$ (hereafter Malkus field). In his study, the slow and the fast modes were recovered from the resulting dispersion relation (see eq. 2.28 in Malkus 1967).

In the ellipsoidal case, the Malkus field is modified to follow the elliptical geostrophic contours. This translates into the background magnetic field $\mathbf{B}_{0,z} = c^2(-y/b^2, x/a^2, 0)^T$ in Cartesian coordinates (e.g. Vidal et al. 2019) and a mean magnetic potential $A_0 = h^3/3$ for the QG model. Due to the lack of any magnetic field component perpendicular to the geostrophic contours, the Malkus field does not permit TM. However, that field allows us to investigate the slow and fast modes in the ellipsoid. We report, for the first time, the dependency of these modes on the equatorial ellipticity

$$\epsilon = \frac{a^2 - b^2}{a^2 + b^2}, \quad (54)$$

where $\epsilon = 0$ corresponds to the axisymmetric case. Here, we investigate the parameter range $\epsilon \in [0, 0.4]$. For all the results shown below, the semi-axis along the rotation axis is kept constant at $c = 1$. The influence of polar flattening has already been investigated previously and is not discussed here (Maffei et al. 2017; Zhang & Liao 2017). Throughout this study, the volume is preserved by setting $a = 1/b$

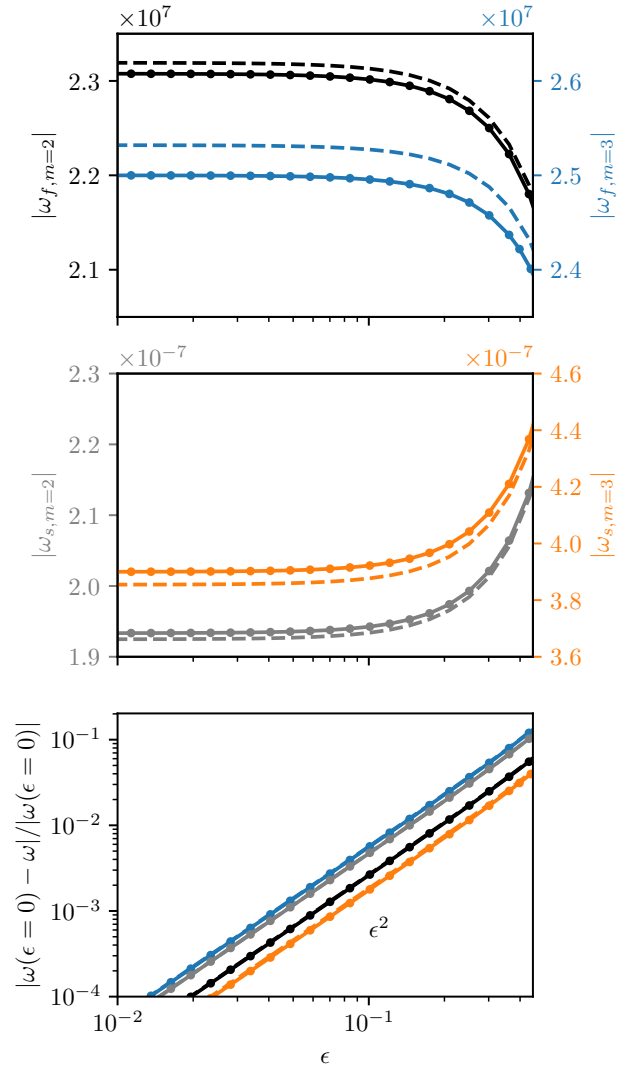


Figure 3. Frequencies $\omega_{f,m}$ of the fast modes (top) and $\omega_{s,m}$ of the slow modes (middle) as a function of ellipticity for radial complexity $l = 1$ and azimuthal wave number $m = 2, 3$. Difference between the frequency as a function of ϵ and the frequency in the sphere with $\epsilon = 0$, normalised by the frequency in the sphere, for the considered fast and slow modes (bottom). The Lehnert number is 10^{-8} . The different models are: QG (solid), hybrid (dots) and 3-D (dashed).

when increasing the ellipticity in the equatorial plane, so that $abc = 1$.

We compute the frequencies of two of the largest-scale fast and slow modes, and track their frequencies as a function of ϵ . The results are shown in Figure 3. The trends of all models agree well. The fast modes decrease in frequency, whereas the slow modes increase their frequency as the ellipticity is increased. The frequency is almost independent of the ellipticity when $\epsilon \ll 1$, and the difference with respect to the spherical values scales as $|\omega(\epsilon=0) - \omega(\epsilon)| \sim \epsilon^2$ for the fast and slow modes (see Figure 3, bottom). This scaling may be anticipated by the relation of the fast and slow modes to the inertial modes in the ellipsoid, showing a similar scaling (compare with equation 3.24 in Vantieghem 2014).

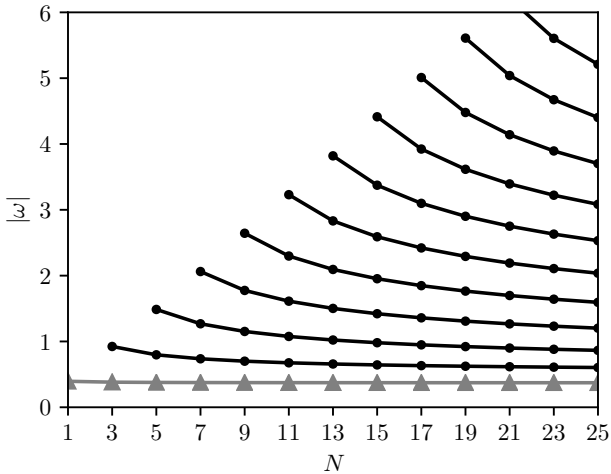


Figure 4. Convergence of frequencies as a function of truncation degree N for a background magnetic field $\mathbf{B}_{0,\text{QG}}$, $\epsilon = 0.42$ and $\text{Le} = 10^{-5}$. Connected lines indicate individual modes. Black lines correspond to TM and the smallest frequency mode (in grey with triangles) is the U_3 -mode.

The Malkus field is completely determined by the geostrophic basis (as introduced in Appendix A). Hence, we do not observe any differences between the QG model (solid line) and the hybrid model (dots). The differences in frequency magnitude between the 3-D model (dashed line) and the QG and hybrid model depend on the modes' complexity (see [Labbé et al. 2015](#); [Maffei et al. 2017](#)). The discrepancies observed between the different models are similar over the entire range of ellipticities considered here ($0 \leq \epsilon \lesssim 0.4$). We are thus confident in using the QG (or hybrid) models for further analysis, as we do not observe strong 3-D effects on the modes by the equatorial ellipticity.

4.2 Torsional Alfvén modes

To drive TM the imposed background magnetic field must have a component perpendicular to the geostrophic contours. For the QG model, we must consider a scalar potential A_0 that is not only a function of h . We choose $A_0 = h^3(1+x)/3$, which yields

$$\mathbf{B}_{0,\text{QG}} = \frac{c^2}{3} \begin{pmatrix} -3(1+x)y/b^2 \\ (3+4x)x/a^2 + y^2/b^2 - 1 \\ yz/b^2 \end{pmatrix}. \quad (55)$$

Since the components of such a magnetic field are no longer linear in the Cartesian coordinates (contrary to the Malkus field), the convergence of the modes depends on the truncation of the maximum polynomial degree. We verify the convergence of the largest scale TM (see black lines in Figure 4). As N is increased more TM with a larger polynomial complexity appear, with one additional TM per two polynomial degrees. This is explained by the introduction of an additional geostrophic basis vector at every second polynomial degree (see [Backus & Rieutord \(2017\)](#), in the sphere and Appendix A in the ellipsoid).

The equatorial and meridional sections of the two lowest frequency (and thus largest scale) TM, calculated using

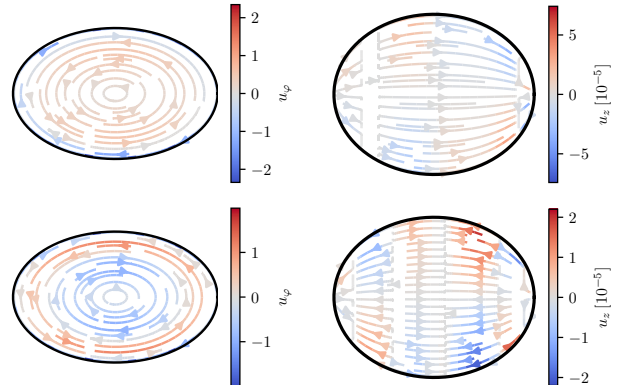


Figure 5. Equatorial sections (left) and meridional sections along the x -axis (right) of the two largest scale TM using $\mathbf{B}_{0,\text{QG}}$, $\epsilon = 0.42$ and $\text{Le} = 10^{-5}$. The colours indicate the velocity along the geostrophic contours u_φ and the vertical velocity u_z , respectively.

$\mathbf{B}_{0,\text{QG}}$ at $N = 7$, are presented in Figure 5 for a strongly deformed ellipsoid with equatorial ellipticity $\epsilon = 0.42$. As in the sphere, the velocities of TM follow the geostrophic contours that are now ellipses. The velocity structure is almost purely horizontal, seen by the ratio of the velocity amplitudes $u_\varphi/u_z \sim 10^5$, where u_φ is the velocity along an elliptical geostrophic contour and u_z is the vertical velocity.

The lowest frequency mode (highlighted in grey triangles in Figure 4) is hereafter referred to as U_3 -mode. It is already present for a truncation degree $N = 1$, where only components linear in the Cartesian coordinates are included. The equatorial and meridional section of the U_3 -mode are presented in Figure 6 for an ellipsoid with equatorial ellipticity of $\epsilon = 0.42$ and $N = 7$. Compared to other TM, it consists almost solely of a velocity with uniform vorticity along the z direction.

4.2.1 Identification of torsional Alfvén modes

When the Lehnert number is not sufficiently small to separate the branches of eigensolutions, as seen for the sphere in Figure 1 at $\text{Le} > 10^{-3}$, a clear identification of TM in the spectrum of eigensolutions is complicated. In Figure 7 we show the dependency of the frequency of the eigensolutions on the Lehnert number for an ellipsoid with $\epsilon = 0.42$. For the TM represented in this Figure, no dependency of the frequency on Le is observed for $\text{Le} \lesssim 10^{-3}$, as in the case of the sphere (compare Figure 1, bottom). Similarly, the U_3 -mode shows no dependency of its frequency on Le

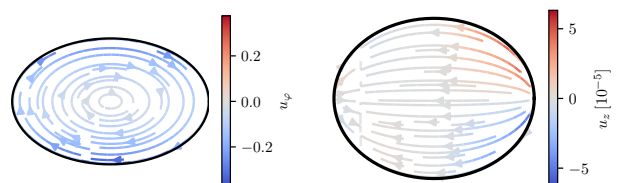


Figure 6. Equatorial section (left) and meridional section along the x -axis (right) of the U_3 -mode using $\mathbf{B}_{0,\text{QG}}$, $\epsilon = 0.42$ and $\text{Le} = 10^{-5}$. The colours indicate the velocity along the geostrophic contours u_φ and the vertical velocity u_z , respectively.

for $Le < 7 \times 10^{-4}$. For $Le \lesssim 10^{-3}$ the TM shown here and the U_3 -mode do not cross any other eigensolutions (and due to their independence of Le they do not cross each other). In this region we have no difficulty in identifying individual TM or the U_3 -mode. When Le is increased to values greater than 10^{-3} , more eigensolutions with frequencies close to the TM or the U_3 -mode exist. Tracking these eigensolutions as a function of Le (as described in Section 3.3) reveals that they can undergo so-called avoided crossings, where two eigensolutions approach each other without ever degenerating. An example of such an avoided crossing is shown in the inset in Figure 7, where the U_3 -mode morphs into the fastest slow mode and vice versa. The two modes exchange their properties, as shown here by the ratio of kinetic to magnetic energy. Such a behaviour has been similarly observed in other geophysical wave studies (Rogister & Valette 2009), even for non-vanishing diffusivities (Triana et al. 2019), or in quantum systems (Rotter 2001). Labbé et al. (2015) chose not to show the results, obtained in the spherical case, for values of Le corresponding to avoided crossing (their Figures 6, 7, 11).

We differentiate in the following the modes, characterised by their physical properties, and the eigenbranches, obtained by continuous tracking of the eigensolutions. This way, we can continue the U_3 -mode and the TM out of the $Le \ll 1$ domain, where they are clearly distinguishable. We have indicated the U_3 mode and TM as well as the fastest slow mode by the coloured lines in the bottom Figure 7.

4.2.2 Ellipticity effects

The dependency of the frequency on the equatorial ellipticity of TM and U_3 -mode is presented in Figure 8 (top). It is observed that, when $\epsilon \lesssim 10^{-1}$, the change of the TM frequency is small and tends to their non-vanishing frequency in the sphere. To be more quantitative, the difference between the frequencies in the ellipsoid and the sphere scales with ϵ for the TM (see Figure 8, bottom).

A very different behaviour is observed for the frequency of the U_3 -mode, since the frequency itself scales with $\epsilon^{1/2}$. This means that the U_3 -mode has a vanishing frequency when $\epsilon = 0$. Also, the ratio of kinetic to magnetic energy of the U_3 -mode scales with ellipticity. These two properties clearly differentiate the U_3 -mode from TM. The restoring force for the U_3 -mode is the pressure force acting on the elliptical boundary. At small ellipticities it is only the magnetic pressure force.

4.2.3 Torque balance

The velocity and magnetic field of an eigensolution $(\tilde{\mathbf{u}}_k, \tilde{\mathbf{B}}_k, \omega_k)$ for a given \mathbf{B}_0 and Le are normalised as

$$\int_{\mathcal{V}} \tilde{\mathbf{u}}_k \cdot \tilde{\mathbf{u}}_k dV + \int_{\mathcal{V}} \tilde{\mathbf{B}}_k \cdot \tilde{\mathbf{B}}_k dV = 1, \quad (56)$$

such that they have a unit energy in dimensionless units. We can then calculate the angular momentum \mathbf{L}_k by inserting \mathbf{u}_k into (6a), and its time derivative is given by $i\omega_k \mathbf{L}_k$. The linearised magnetic pressure torque is given by

$$\Gamma_{\text{pm}} = - \int_{\mathcal{V}} \mathbf{r} \times \nabla \left(\tilde{\mathbf{B}} \cdot \mathbf{B}_0 \right) dV, \quad (57)$$

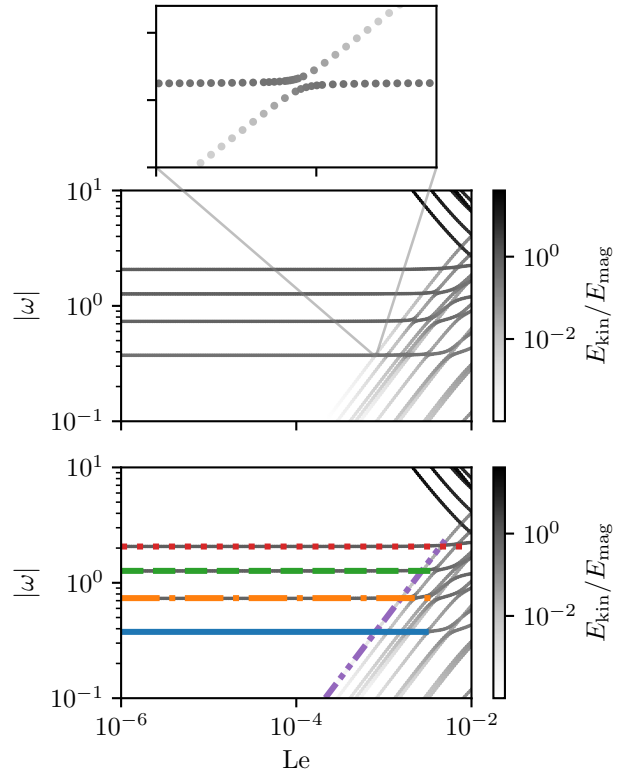


Figure 7. Frequency of eigensolutions as a function of Lehnert number for $\epsilon = 0.42$, with colours indicating the ratio of kinetic to magnetic energy (top). The inset shows an avoided crossing of the U_3 -mode and the fastest slow mode, with dots indicating individual steps of the tracking algorithm. The frequencies of TM (orange dash-dotted), U_3 -mode (blue solid) and the fastest slow mode (purple dash-dot-dotted) are highlighted in the bottom Figure.

and $\Gamma_{\text{pm},k}$ follows by inserting $\tilde{\mathbf{B}}_k$ and \mathbf{B}_0 . The hydrodynamic pressure torque (6b) is calculated by reconstructing the pressure gradient, which cannot be done from the velocity field only. We reconstruct it instead by inserting $\tilde{\mathbf{u}}_k$, $\tilde{\mathbf{B}}_k$ and \mathbf{B}_0 in the momentum equation (47a).

The axial torques in a strongly deformed ellipsoid with $a, b, c = 1.25, 0.8, 1$ (i.e. $\epsilon = 0.42$) are shown in Figure 9. We find non-vanishing torques along the rotation axis for slow modes ($10^{-5} < \omega < 10^{-2}$), TM ($10^{-1} < \omega < 10$) and the fast modes ($\omega > 10^2$). For many modes the hydrodynamic, magnetic and total pressure (sum of hydrodynamic and magnetic pressure) torques do not vanish. For most fast modes $\Gamma_{\text{p},z}$ balances $\Gamma_{\text{pm},z}$ exactly. In case $\Gamma_{\text{p},z}$ is not exactly balanced by $\Gamma_{\text{pm},z}$, the total pressure torque is in balance with the non-vanishing change in angular momentum ωL_z , in agreement with equation (9). For example, the TM with largest scale (and smallest frequency $\omega = 0.737$) has $\Gamma_{\text{p},z} = -1.285 + 1.414i$, $\Gamma_{\text{pm},z} = 1.159 - 1.275i$ and $i\omega L_z = -0.126 + 0.139i$. Our results show that TM yield pressure torques much larger than the slow and fast modes.

Ivers (2017) demonstrated that, in the ellipsoid, only flows of uniform vorticity carry angular momentum. They

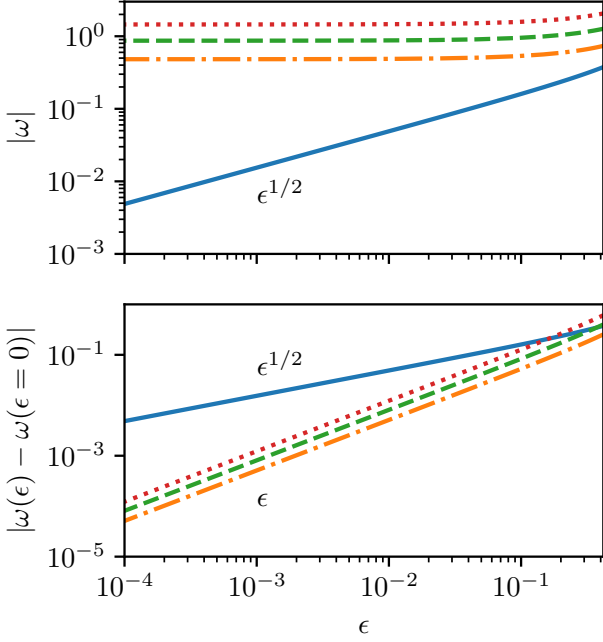


Figure 8. Frequencies of TM (orange dash-dotted, green dashed and red dotted) and the U_3 -mode (blue solid) as a function of ellipticity ϵ (top). Difference between the frequency as a function of ϵ and the frequency in the sphere with $\epsilon = 0$ (bottom). The Lehnert number is $\text{Le} = 10^{-5}$.

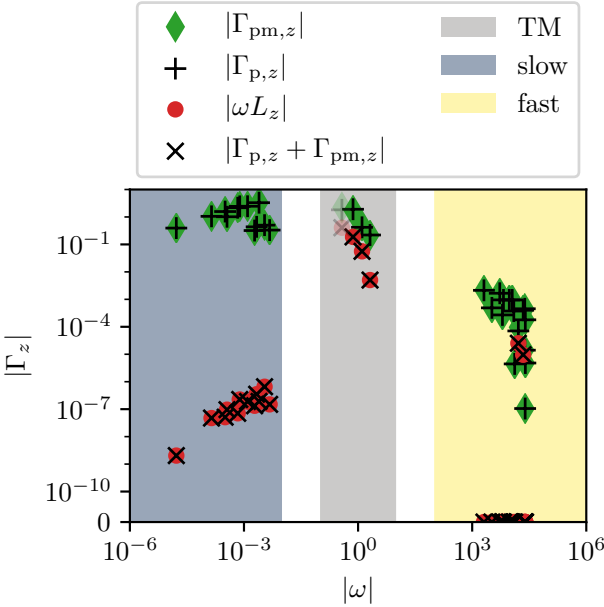


Figure 9. The z component of the torques for the background magnetic field with truncating degree $N = 7$, $\epsilon = 0.42$ and $\text{Le} = 10^{-5}$. The U_3 -mode is displayed slightly transparent.

are given by

$$\hat{\mathbf{u}}_1 = \begin{pmatrix} 0 \\ -z/c^2 \\ y/b^2 \end{pmatrix}, \quad \hat{\mathbf{u}}_2 = \begin{pmatrix} -z/c^2 \\ 0 \\ x/a^2 \end{pmatrix}, \quad \hat{\mathbf{u}}_3 = \begin{pmatrix} -y/b^2 \\ x/a^2 \\ 0 \end{pmatrix}, \quad (58)$$

with a spatially uniform vorticity in the x , y and z directions, respectively. Therefore, we determine if the modes do contain such uniform vorticity components and whether or not it accounts for the non-vanishing angular momentum. To this end, we must project the eigensolutions onto velocities (58) and the resulting angular momentum of the i -th uniform vorticity component of an eigensolution with velocity \mathbf{u}_k is given by

$$\hat{L}_{i,k} = \frac{1}{\sqrt{\int \hat{\mathbf{u}}_i \cdot \hat{\mathbf{u}}_i dV}} \int_{\mathcal{V}} (\hat{\mathbf{u}}_i \cdot \tilde{\mathbf{u}}_k) (\hat{\mathbf{u}}_i \times \mathbf{r}) \cdot \mathbf{1}_i dV. \quad (59)$$

For all modes we find (within machine precision) that $L_{z,k} = \hat{L}_{3,k}$, in agreement with the predictions by [Ivers \(2017\)](#).

The U_3 -mode, shown slightly transparent in [Figure 9](#), has a velocity almost exactly equal to $\hat{\mathbf{u}}_3$ (thus the name U_3 -mode). It is associated with the largest torque. However, the time scale at which this torque acts increases as the ellipticity is decreased to more geophysically relevant values, whereas it remains the same for TM.

4.2.4 Torque variation with the ellipticity and Lehnert number

We show in [Figure 10](#) the dependency on the ellipticity of the angular momentum in z (top), and the associated changes (bottom). The angular momentum scales with ϵ for the TM, and with $\epsilon^{1/2}$ for the U_3 -mode. Since the frequency is almost independent of ϵ for the TM, and scales with $\epsilon^{1/2}$ for the U_3 -mode, the change in angular momentum scales with ϵ for all modes. A vanishing change in angular momentum is necessary to satisfy the torque balance in the sphere, where the pressure torque vanishes exactly. Departures from the aforementioned scalings are only observed for strongly deformed ellipsoids (i.e. $\epsilon > 0.1$). For TM with higher frequencies, the spatial complexity of the modes increases and their angular momentum and the change in angular momentum decreases.

In [Figure 11](#) we show the evolution of the angular momentum and change in angular momentum of TM and the U_3 -mode as a function of the Lehnert number. For $\text{Le} \lesssim 10^{-3}$ we observe no dependency on Le for the angular momentum. Thus, because the frequency is also independent of Le (see [Figure 7](#)), there is no dependency of the change in angular momentum on Le and the total pressure torque must scale in the same way.

The frequencies of the eigenbranches are close-by when $\text{Le} > 10^{-3}$, and they undergo the previously discussed avoided crossings. However, we are still able to identify the TM and U_3 -mode by their frequency and angular momentum when $\text{Le} \ll 1$ (see [Figure 11](#)). To check the influence of truncation on the results, we have computed the change in angular momentum of all the eigensolutions as a function of Le for the truncation degree $N = 11$. The U_3 mode and the TM can be well characterised by their angular momentum (see [Figure 12](#)). Comparison between our results for $N = 7$ and $N = 11$ makes us confident that our angular momentum calculations for U_3 and the largest scale TM are converged at $N = 7$.

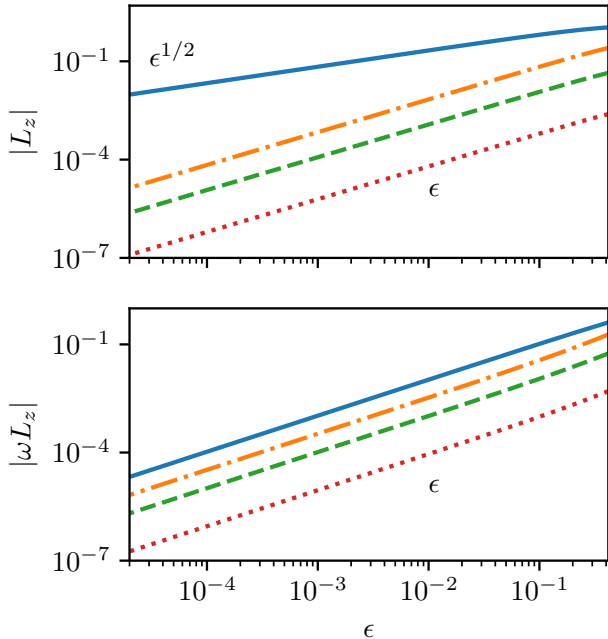


Figure 10. Axial angular momentum (top) and its change (bottom) of TM and the U_3 -mode as a function of ellipticity for the background magnetic field $\mathbf{B}_{0,\text{QG}}$ and $\text{Le} = 10^{-5}$. The colours correspond to those in Figure 8.

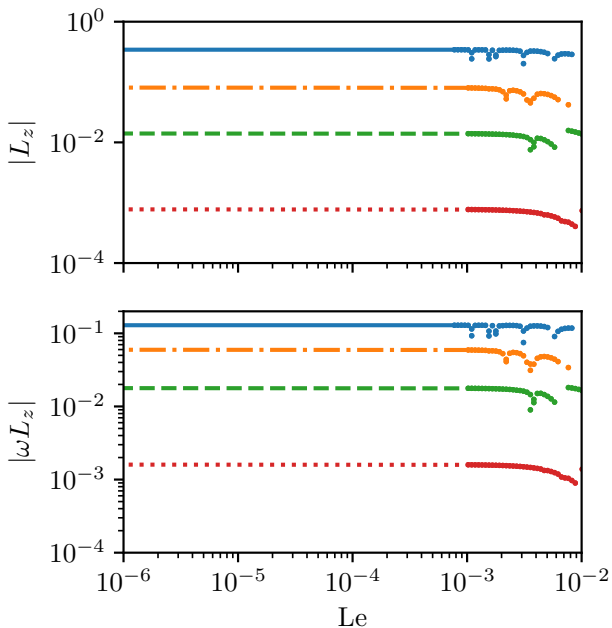


Figure 11. Axial angular momentum (top) and its change (bottom) of TM and the U_3 -mode for the background magnetic field $\mathbf{B}_{0,\text{QG}}$ and $a, b, c = 1.25, 0.8, 1$ ($\epsilon = 0.42$) with $N = 7$. At $\text{Le} \gtrsim 10^{-3}$, where eigensolutions are influenced by avoided crossings, we have identified the modes by choosing a frequency within $\pm 10\%$ and an angular momentum within $\pm 50\%$ of the frequency and angular momentum at $\text{Le} \ll 1$. The colours correspond to those in Figure 8.

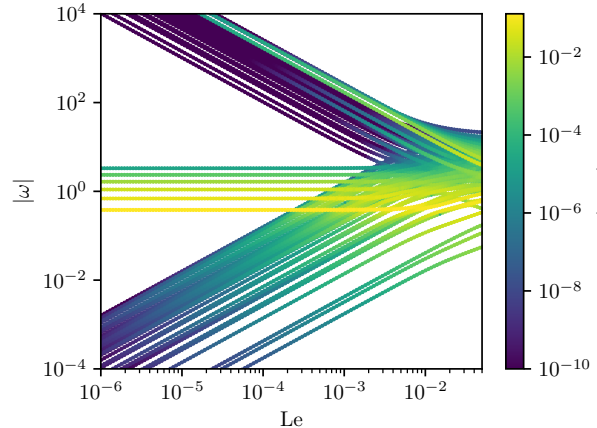


Figure 12. Change of axial angular momentum for the QG model with $\mathbf{B}_{0,\text{QG}}$ and $N = 11$. The full spectrum of eigensolutions is computed at incremental steps of Le , without tracking an individual eigensolution.

To check the generality of these results, we have considered a 3-D magnetic field in the hybrid model. The results are presented in Appendix B. No qualitative differences with the results of the QG model are found, even if the background magnetic field has a different topology. We follow from this that our results extend to more complex background magnetic field geometries. Further verification was done using a fully 3-D model, where no QG assumption is made on the velocity (not shown).

5 DISCUSSION AND CONCLUSIONS

5.1 Pressure torque and angular momentum of torsional Alfvén modes in ellipsoids

We have found that TM in the ellipsoid can have a non-vanishing angular momentum. Their angular momentum is fully accounted for by their uniform vorticity flow component along the rotation axis. This fully agrees with Ivers (2017), who proved that only uniform vorticity flows have non-zero angular momentum. In the hydrodynamic case (without magnetic field), only the geostrophic mode can have a non-vanishing axial angular momentum. Since its frequency is zero, the change in axial angular momentum vanishes. All other inertial modes in a non-conductive fluid enclosed in an ellipsoid are orthogonal to the geostrophic mode and no inertial mode can produce a net axial torque acting on the boundary. In MHD, the modes have a magnetic component and we lose the orthogonality properties between the velocity components. It is well known that TM exist, whose frequency is non-zero, with a dominant velocity component along the geostrophic contours. We have shown that these TM keep following the geostrophic contours for an ellipsoidal domain, and carry angular momentum through their uniform vorticity component when non-axisymmetry is present. This change in angular momentum must be balanced by the total pressure torque, as the Coriolis torque is exactly zero along the rotation axis and in our model the magnetic tension torque Γ_b also vanishes. Our results confirm this balance, and there are modes for which the

hydrodynamic pressure torque is larger than the magnetic pressure torque. It is worth discussing whether our results extend to the case of a perfectly insulating boundary, where the magnetic tension torque $\mathbf{\Gamma}_b$ exactly balances the magnetic pressure torque $\mathbf{\Gamma}_{pm}$. Then, only the hydrodynamic pressure torque can balance changes in angular momentum. Investigating perfectly insulating boundaries remains a future problem as it is inherently impossible by our methodology and out of the scope of this work.

We have shown that the frequency of TM remains independent of the Lehnert number, as is the case in the sphere. The angular momentum is also independent of the Lehnert number, and thus is the change of angular momentum and the associated pressure torque. The frequency of TM is also almost unaffected by small ellipticities. The angular momentum (and its change) of TM scales as ϵ , so that it vanishes in the sphere (as it should).

In addition to the TM, we observed the particular U_3 -mode, mainly of uniform vorticity in the axial direction, carrying angular momentum. For a strongly deformed ellipsoid with $\epsilon = \mathcal{O}(10^{-1})$ the frequency of the U_3 -mode happens to be in the range of TM. As for TM the frequency and the angular momentum of the U_3 -mode does not depend on Le for small enough Le. However, in contrast to TM its frequency scales with $\epsilon^{1/2}$, a mode behaviour so far unknown to the authors. The U_3 -mode is thus geostrophic in the sphere, with a vanishing frequency. Its frequency also vanishes for the hydrodynamic case, regardless of the ellipticity. A magnetic field with a component perpendicular to the geostrophic contours is needed in addition to non-axisymmetry to drive this mode.

Another interesting application of our model is the extension to more complex geometries (as long as closed geostrophic contours exist). The derived equations are indeed independent of the (possibly non-orthogonal) coordinate system. The ellipsoidal case presented here can be used as a benchmark for follow up work in this direction. We have additionally presented the first hybrid model, with the velocity in the QG assumption and a 3-D magnetic field. A property highly desirable in core flow dynamics, where a columnar flow model seems appropriate, but the magnetic field is clearly three dimensional (e.g. [Schaeffer et al. 2017](#)).

5.2 Geophysical implications

Our results suggest that TM in the Earth's core, which have periods on the scale of a few years, exert a pressure torque onto the solid mantle, provided the CMB is non-axisymmetric. The observed variations in the LOD are $\mathcal{O}(10^{-4})$ s at the 6 yr period ([Gillet et al. 2015](#)), which corresponds to a change in angular momentum $\mathcal{O}(10^{16})$ Nm. To compare this to the torques of TM calculated here, we redimensionalise our numerical results by assuming a characteristic velocity $u_0 = 5 \times 10^{-6}$ m/s of TM (see Figure 10 in [Gillet et al. 2015](#)). We match the frequencies of the calculated TM to the 6 yr period, so that a characteristic background magnetic field strength B_0 and similarly Le is defined. For an ellipticity $\epsilon = 10^{-3}$, estimated for Earth ([Sze & van der Hilst 2003](#); [Koper et al. 2003](#)), the resulting values are presented in Table 1. The frequency conversion to match a 6 yr period yields a characteristic magnetic field strength of $B_0 \sim 4 - 30$ mT, hence a Lehnert number $Le = \mathcal{O}(10^{-4})$.

Table 1. Estimation of change in angular momentum of TM for Earth's core, with $\epsilon = 10^{-3}$. The TM are normalised to have a period $T = 6$ yr. The characteristic TM velocity is set to $u_0 = 5 \times 10^{-6}$ m/s.

Model	ω	L_z	Le[10^{-4}]	B_0 [mT]	ωL_z [Nm]
QG	0.48	113	9.5	29.5	9.5×10^{14}
QG	0.865	18.3	5.28	16.4	1.54×10^{14}
QG	1.45	0.92	3.15	9.8	7.76×10^{12}
Hybrid	1.14	87.4	4.02	12.5	7.37×10^{14}
Hybrid	2.06	9.24	2.22	6.89	7.79×10^{13}
Hybrid	3.34	0.35	1.37	4.25	2.95×10^{12}

These values are in agreement with what is expected for the Earth's outer core ([Gillet et al. 2010](#)). The resulting change in angular momentum, and thus the pressure torque, is at most $\mathcal{O}(10^{14})$ Nm for all modes. These values are two orders below the value needed to explain the variation of the LOD on the 6 yr period. This result can be better understood from a dimensional analysis of the pressure. First, the pressure varies linearly with the TM velocity. Second, the TM are independent of Ω . Therefore, the pressure associated to the velocity of TM scales with $p_0 \sim \rho u_0 u_A = \mathcal{O}(10^{-3})$ Pa. With this value, we verify that the resulting hydrodynamic pressure torque is $\mathcal{O}(10^{14})$ Nm.

In order to make the pressure torque significant, we need deviations from geostrophy so that pressure depends on Ω . This may happen in the presence of non-closed geostrophic contours. Then, 'pseudo-geostrophic' modes are replaced by Rossby modes, whose properties depend on Ω . These Rossby modes are not steady and possess the mean circulation included in the geostrophic mode otherwise ([Greenspan 1968](#)). Thus, Rossby modes driven by the magnetic field may play an important role for the pressure torque on a non-spherical boundary, where non-closed contours exist. It is easy to imagine this scenario in the presence of an inner core or at the CMB of the core, with a trough directed inwards at the equator. Stratification at the upper outer core may further increase the efficiency of the topographic torque ([Braginsky 1998](#); [Glane & Buffett 2018](#); [Jault 2020](#)).

Another hypothetical geophysical application is the explanation of the very long period variations in the LOD through the U_3 -mode. These variations are $\mathcal{O}(10^{-3})$ s and have a period of around 1500 yr ([Stephenson et al. 1995](#); [Dumberry & Bloxham 2006](#)). The U_3 -mode in our model has a period of 1800 yr for $Le = 10^{-4}$ and an ellipticity of $\epsilon = 10^{-3}$. The U_3 -mode could therefore be an explanation for these long period variations, but this remains a very speculative idea.

ACKNOWLEDGMENTS

FG was partly funded by Labex OSUG@2020 (ANR10 LABX56). JN was partly funded by SNF Grant #200021.185088. JV was partly funded by STFC Grant ST/R00059X/1. This work was supported by a grant from the Swiss National Supercomputing Centre (CSCS) under project ID s872. This work has been carried out with financial support from CNES (Centre National d'Études Spatiales, France). Support is acknowledged from the European

Space Agency through contract 4000127193/19/NL/IA. The authors like to thank two anonymous reviewers for their help in improving this manuscript.

REFERENCES

- Abarca del Rio, R., Gambis, D., & Salstein, D. A., 2000. Interannual signals in length of day and atmospheric angular momentum, *Annales Geophysicae*, **18**(3), 347–364.
- Aris, R., 1989. *Vectors, Tensors and the Basic Equations of Fluid Mechanics*, Dover.
- Backus, G. & Rieutord, M., 2017. Completeness of inertial modes of an incompressible inviscid fluid in a corotating ellipsoid, *Phys. Rev. E*, **95**(5), 053116.
- Backus, G., Parker, R., & Constable, C., 1996. *Foundations of Geomagnetism*, Cambridge University Press.
- Bardsley, O. P., 2018. Could hydrodynamic Rossby waves explain the westward drift?, *Proc. R. Soc. A*, **474**, 20180119.
- Bezanson, J., Edelman, A., Karpinski, S., & Shah, V. B., 2017. Julia: A Fresh Approach to Numerical Computing, *SIAM Review*, **59**(1), 65–98.
- Braginsky, S. I., 1970. Torsional magnetohydrodynamics vibrations in the Earth’s core and variations in day length, *Geomagn. Aeron.*, **10**, 3–12.
- Braginsky, S. I., 1998. Magnetic Rossby waves in the stratified ocean of the core, and topographic core-mantle coupling, *Earth, Planets and Space*, **50**(8), 641–649.
- Buffett, B. A., 1996a. Gravitational oscillations in the length of day, *Geophys. Res. Lett.*, **23**(17), 2279–2282.
- Buffett, B. A., 1996b. A mechanism for decade fluctuations in the length of day, *Geophys. Res. Lett.*, **23**(25), 3803–3806.
- Brenzung, J., Holschneider, M., Wicht, J., Sanchez, S., & Lesur, V., 2018. Modeling and Predicting the Short-Term Evolution of the Geomagnetic Field, *Journal of Geophysical Research: Solid Earth*, **123**(6), 4539–4560.
- Canet, E., Finlay, C. C., & Fournier, A., 2014. Hydromagnetic quasi-geostrophic modes in rapidly rotating planetary cores, *Phys. Earth Planet. Inter.*, **229**(Supplement C), 1–15.
- Davidson, P. A., 2016. *Introduction to Magnetohydrodynamics*, Cambridge University Press, Cambridge.
- Davies, C. J., Stegman, D. R., & Dumberry, M., 2014. The strength of gravitational core-mantle coupling, *Geophys. Res. Lett.*, **41**(11), 3786–3792.
- Dumberry, M. & Bloxham, J., 2006. Azimuthal flows in the Earth’s core and changes in length of day at millennial timescales, *Geophys. J. Int.*, **165**(1), 32–46.
- Gans, R. F., 1971. On hydrodynamic oscillations in a rotating cavity, *J. Fluid Mech.*, **50**, 449–467.
- Gastine, T., 2019. pizza: an open-source pseudo-spectral code for spherical quasi-geostrophic convection, *Geophys. J. Int.*, **217**(3), 1558–1576.
- Gillet, N., Jault, D., Canet, E., & Fournier, A., 2010. Fast torsional waves and strong magnetic field within the Earth’s core, *Nature*, **465**(7294), 74–77.
- Gillet, N., Schaeffer, N., & Jault, D., 2011. Rationale and geophysical evidence for quasi-geostrophic rapid dynamics within the Earth’s outer core, *Physics of the Earth and Planetary Interiors*, **187**(3), 380–390.
- Gillet, N., Jault, D., & Finlay, C. C., 2015. Planetary gyre, time-dependent eddies, torsional waves, and equatorial jets at the Earth’s core surface, *Journal of Geophysical Research: Solid Earth*, **120**(6), 3991–4013.
- Gillet, N., Jault, D., & Canet, E., 2017. Excitation of travelling torsional normal modes in an Earth’s core model, *Geophys. J. Int.*, **210**(3), 1503–1516.
- Glane, S. & Buffett, B., 2018. Enhanced Core-Mantle Coupling Due to Stratification at the Top of the Core, *Front. Earth Sci.*, **6**.
- Greenspan, H. P., 1968. *The Theory of Rotating Fluids*, Cambridge University Press.
- Gross, R. S., 2015. 3.09 - Earth Rotation Variations CoreLong Period, in *Treatise on Geophysics (Second Edition)*, pp. 215–261, ed. Schubert, G., Elsevier.
- Guervilly, C., Cardin, P., & Schaeffer, N., 2019. Turbulent convective length scale in planetary cores, *Nature*, **570**(7761), 368.
- Hide, R., 1966. Free hydromagnetic oscillations of the Earth’s core and the theory of the geomagnetic secular variation, *Philos. T. R. Soc. A*, **259**(1107), 615–647.
- Hide, R., 1969. Interaction between the Earth’s Liquid Core and Solid Mantle, *Nature*, **222**(5198), 1055–1056.
- Holme, R. & de Viron, O., 2013. Characterization and implications of intradecadal variations in length of day, *Nature*, **499**(7457), 202–204.
- Ivers, D., 2017. Enumeration, orthogonality and completeness of the incompressible Coriolis modes in a tri-axial ellipsoid, *Geophys. Astrophys. Fluid Dyn.*, **111**(5), 333–354.
- Jault, D., 2003. Electromagnetic and topographic coupling, and LOD variations, in *Earth’s Core and Lower Mantle*, pp. 56–76, eds Zhang, K., Soward, A., & Jones, C., London: CRC press.
- Jault, D., 2020. Tangential stress at the core-mantle interface, *Geophys. J. Int.*, **221**(2), 951–967.
- Jault, D. & Le Mouél, J.-L., 1990. Core-mantle boundary shape: constraints inferred from the pressure torque acting between the core and the mantle, *Geophys. J. Int.*, **101**(1), 233–241.
- Jault, D., Gire, C., & Le Mouél, J.-L., 1988. Westward drift, core motions and exchanges of angular momentum between core and mantle, *Nature*, **333**, 353–353.
- Kerswell, R. R., 1994. Tidal excitation of hydromagnetic waves and their damping in the Earth, *J. Fluid Mech.*, **274**, 219–241.
- Koper, K. D., Pyle, M. L., & Franks, J. M., 2003. Constraints on aspherical core structure from PKiKP-PcP differential travel times, *Journal of Geophysical Research: Solid Earth*, **108**(B3).
- Labbé, F., Jault, D., & Gillet, N., 2015. On magnetostrophic inertia-less waves in quasi-geostrophic models of planetary cores, *Geophys. Astrophys. Fluid Dyn.*, **109**(6), 587–610.
- Lebovitz, N. R., 1989. The stability equations for rotating, inviscid fluids: Galerkin methods and orthogonal bases, *Geophys. Astrophys. Fluid Dyn.*, **46**(4), 221–243.
- Liao, X. & Zhang, K., 2010. A new Legendre-type polynomial and its application to geostrophic flow in rotating fluid spheres, *Proc. R. Soc. A*, **466**(2120), 2203–2217.
- Maffei, S., Jackson, A., & Livermore, P. W., 2017. Characterization of columnar inertial modes in rapidly rotating spheres and spheroids, *Proc. R. Soc. A*, **473**(2204).
- Malkus, W. V. R., 1967. Hydromagnetic planetary waves, *J. Fluid Mech.*, **28**(4), 793–802.
- Mound, J. E. & Buffett, B. A., 2006. Detection of a gravitational oscillation in length-of-day, *Earth and Planetary Science Letters*, **243**(3), 383–389.
- Munk, W. H. & MacDonald, G. J. F., 1960. *The Rotation of the Earth: A Geophysical Discussion*, Cambridge University Press.
- Pozzo, M., Davies, C., Gubbins, D., & Alf, D., 2014. Thermal and electrical conductivity of solid iron and iron-silicon mixtures at Earth’s core conditions, *Earth and Planetary Science Letters*, **393**, 159–164.
- Rieutord, M. & Valdettaro, L., 1997. Inertial waves in a rotating spherical shell, *J. Fluid Mech.*, **341**, 77–99.
- Roberts, P. H., 1972. Electromagnetic Core-Mantle Coupling, *J. Geomagn. Geoelectr.*, **24**(2), 231–259.
- Roberts, P. H. & Aurnou, J. M., 2012. On the theory of core-mantle coupling, *Geophys. Astrophys. Fluid Dyn.*, **106**(2), 157–230.
- Rogister, Y. & Valette, B., 2009. Influence of liquid core dynam-

- ics on rotational modes, *Geophys. J. Int.*, **176**(2), 368–388.
- Rotter, I., 2001. Dynamics of quantum systems, *Physical Review E*, **64**(3), 036213.
- Schaeffer, N. & Jault, D., 2016. Electrical conductivity of the lowermost mantle explains absorption of core torsional waves at the equator, *Geophys. Res. Lett.*, **43**(10), 4922–4928.
- Schaeffer, N., Jault, D., Nataf, H.-C., & Fournier, A., 2017. Turbulent geodynamo simulations: a leap towards Earths core, *Geophys. J. Int.*, **211**(1), 1–29.
- Stephenson, F. R., Morrison, L. V., & Smith, F. T., 1995. Long-term fluctuations in the Earths rotation: 700 BC to AD 1990, *Philosophical Transactions of the Royal Society of London. Series A: Physical and Engineering Sciences*, **351**(1695), 165–202.
- Sze, E. K. M. & van der Hilst, R. D., 2003. Core mantle boundary topography from short period PcP, PKP, and PKKP data, *Phys. Earth Planet. Inter.*, **135**(1), 27–46.
- Triana, S. A., Requier, J., Trinh, A., & Dehant, V., 2019. The coupling between inertial and rotational eigenmodes in planets with liquid cores, *Geophys. J. Int.*, **218**(2), 1071–1086.
- Vantieghem, S., 2014. Inertial modes in a rotating triaxial ellipsoid, *Proc. R. Soc. A*, **470**, 20140093.
- Vantieghem, S., Cébron, D., & Noir, J., 2015. Latitudinal libration driven flows in triaxial ellipsoids, *J. Fluid Mech.*, **771**, 193–228.
- Vidal, J. & Cébron, D., 2017. Inviscid instabilities in rotating ellipsoids on eccentric Kepler orbits, *J. Fluid Mech.*, **833**, 469–511.
- Vidal, J. & Schaeffer, N., 2015. Quasi-geostrophic modes in the Earth’s fluid core with an outer stably stratified layer, *Geophys. J. Int.*, **202**(3), 2182–2193.
- Vidal, J., Cébron, D., & Schaeffer, N., 2016. Diffusionless hydro-magnetic modes in rotating ellipsoids: a road to weakly non-linear models?, in *Comptes-Rendus de la 19e Rencontre du Non-Linéaire*.
- Vidal, J., Cébron, D., ud Doula, A., & Alecian, E., 2019. Fossil field decay due to nonlinear tides in massive binaries, *Astron. Astrophys.*, **629**, A142.
- Vidal, J., Su, S., & Cébron, D., 2020. Compressible fluid modes in rigid ellipsoids: towards modal acoustic velocimetry, *J. Fluid Mech.*, **885**, A39.
- Watkins, A., Fu, Y., & Gross, R., 2018. Earths subdecadal angular momentum balance from deformation and rotation data, *Scientific Reports*, **8**(1), 13761.
- Wijs, G. A. d., Kresse, G., Voadlo, L., Dobson, D., Alf, D., Gillan, M. J., & Price, G. D., 1998. The viscosity of liquid iron at the physical conditions of the Earth’s core, *Nature*, **392**(6678), 805.
- Wu, C.-C. & Roberts, P. H., 2011. High order instabilities of the Poincaré solution for precessionally driven flow, *Geophys. Astrophys. Fluid Dyn.*, **105**(2-3), 287–303.
- Zhang, K. & Liao, X., 2017. *Theory and Modeling of Rotating Fluids: Convection, Inertial Waves and Precession*, Cambridge University Press.

APPENDIX A: GEOSTROPHIC FLOW DESCRIBED BY A STREAM FUNCTION

The geostrophic part of the velocity can be regarded as the average over a geostrophic column. This is equivalent to considering a stream function

$$\tilde{\psi}(h) = \frac{\oint \psi(h, \varphi) d\varphi}{\oint d\varphi}, \quad (\text{A.1})$$

depending only on the geostrophic column height h . Here, we have chosen the coordinates (h, φ, z) conveniently, such

that φ is the coordinated along a closed geostrophic contour of constant h and $z \in [-h, h]$ is along the rotation axis. In the axisymmetric case these coordinates are identical to the cylindrical coordinates. In the generic case, with arbitrarily shaped geostrophic contours, we have to apply curvilinear coordinates, that are not necessarily orthogonal. For non-orthogonal coordinates the dual, covariant and contravariant, bases \mathbf{g}_i and \mathbf{g}^i are needed. We refer the reader to [Aris \(1989\)](#) for more details on non-orthogonal curvilinear coordinates.

Inserting [\(A.1\)](#) into [\(16\)](#) the geostrophic velocity is given by

$$\mathbf{u}_G = \nabla \tilde{\psi}(h) \times \nabla \left(\frac{z}{h} \right) \quad (\text{A.2a})$$

$$= u_G(h, \varphi) \mathbf{g}_2, \quad (\text{A.2b})$$

with $u_G(h, \varphi) = (Jh)^{-1} \frac{\partial \tilde{\psi}}{\partial h}$ and the covariant basis vector in φ -direction \mathbf{g}_2 . Here, $J(h, \varphi, z) = \det(g_{ij})$ is the Jacobian of the coordinate mapping. The metric elements are given as $g_{ij} = \mathbf{g}_i \cdot \mathbf{g}_j$. In case of the sphere or the ellipsoid $J = J(h)$. The geostrophic pressure p_G is well defined and depends on h only

$$2\rho \mathbf{u}_G \times \boldsymbol{\Omega} = -\nabla p_G \quad (\text{A.3a})$$

$$\Leftrightarrow \frac{2\rho \Omega}{h} \frac{\partial \tilde{\psi}}{\partial h} = \frac{\partial p_G}{\partial h}. \quad (\text{A.3b})$$

To construct a basis of geostrophic velocities $\mathbf{u}_{G,i}$ being polynomial in the Cartesian coordinates the stream function $\tilde{\psi}_i(h)$ has to take the form

$$\tilde{\psi}_i(h) = \frac{1}{3} h^{3+2i}, \quad (\text{A.4})$$

where $h^2 = c^2(1 - x^2/a^2 - y^2/b^2)$. The basis of geostrophic velocities is given as

$$\mathbf{u}_{G,i} = \frac{1}{h} \nabla \tilde{\psi}_i \times \mathbf{1}_z = \frac{1}{3} (3 + 2i) h^{2i} \nabla g \times \mathbf{1}_z, \quad (\text{A.5})$$

with $\nabla g = -c^2(x/a^2, y/b^2, 0)^\top$.

APPENDIX B: HYBRID MODEL

In the hybrid (or fully 3-D) model the background magnetic fields are less restricted, and we select an admissible field from appendix A in [Wu & Roberts \(2011\)](#). Namely, we consider the magnetic field

$$\mathbf{B}_{0,\text{hyb}} = \begin{pmatrix} xy \\ -2b^2(x^2/a^2 + z^2/c^2) + b^2 - y^2 \\ yz \end{pmatrix}, \quad (\text{B.1})$$

named \mathbf{v}_8 in the quadratic basis of [Wu & Roberts \(2011\)](#). We choose this field, as it clearly goes beyond the magnetic field [\(55\)](#) while keeping the maximum polynomial degree sufficiently low to ensure convergence.

The U_3 -mode and the two largest scale TM are presented in [Figure A1](#). Even though the background magnetic field considered here is topologically speaking very different to $\mathbf{B}_{0,\text{QG}}$, the modes show a clear spatial similarity (compare [Figure 5](#)). The axial torques are presented in [Figure A2](#). No qualitative difference to the QG model is observed.

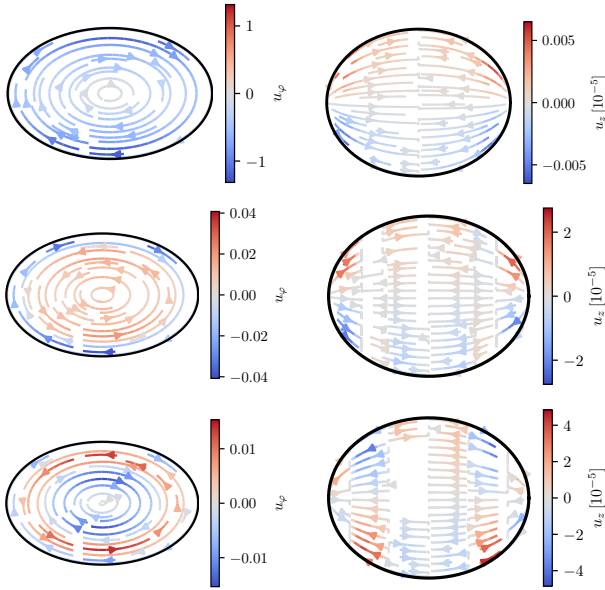


Figure A1. Equatorial sections (left) and meridional sections along the x -axis (right) of the U_3 -mode (top) and the two largest TM (middle and bottom) using $\mathbf{B}_{0,\text{hyb}}$, $\epsilon = 0.42$ and $\text{Le} = 10^{-5}$. The colours indicate the velocity along the geostrophic contours u_φ and the vertical velocity u_z , respectively.

For modes with non-vanishing change in angular momentum the total pressure torque balances it. Again, the U_3 -mode carries the largest angular momentum and for some slow modes and fast modes the change in angular momentum is also non-vanishing.

The dependency of the frequency, angular momentum and the change of angular momentum of the U_3 -mode and TM on the ellipticity is shown in Figure A3. The same scalings in ϵ are observed for the U_3 -mode and the TM compared to the QG case.

Finally, we present the dependency of the angular momentum and its time derivative of the TM and the U_3 -mode in Figure A4. As in the QG case, no dependency is observed. In comparison to the QG case, the U_3 -mode and the TM seem to be less influenced by avoided crossings at $\text{Le} > 10^{-3}$ (compare to Figure 11).

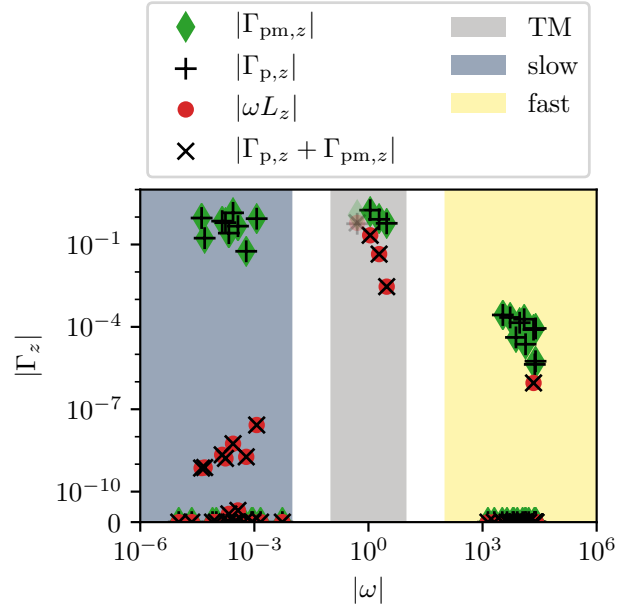


Figure A2. The z component of the torques using $\mathbf{B}_{0,\text{hyb}}$, $\epsilon = 0.42$ and $\text{Le} = 10^{-5}$ with truncating degree $N = 9$.

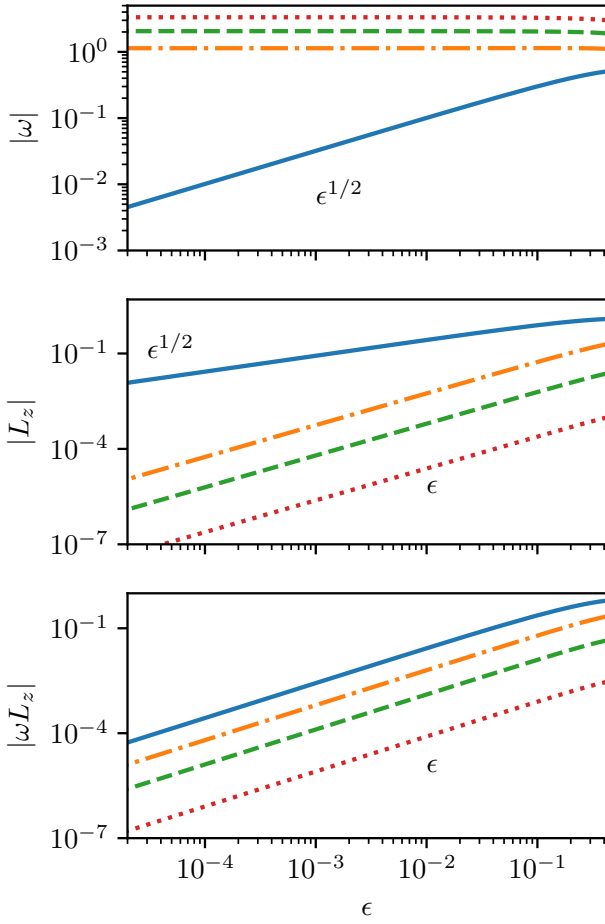


Figure A3. Frequency (top), axial angular momentum (middle) and change in axial angular momentum (bottom) of the three largest scale TM (orange dash-dotted, green dashed and red dotted) and the U_3 -mode (blue solid) for $\mathbf{B}_{0,\text{hyb}}$ and $\text{Le} = 10^{-5}$ using the hybrid model.

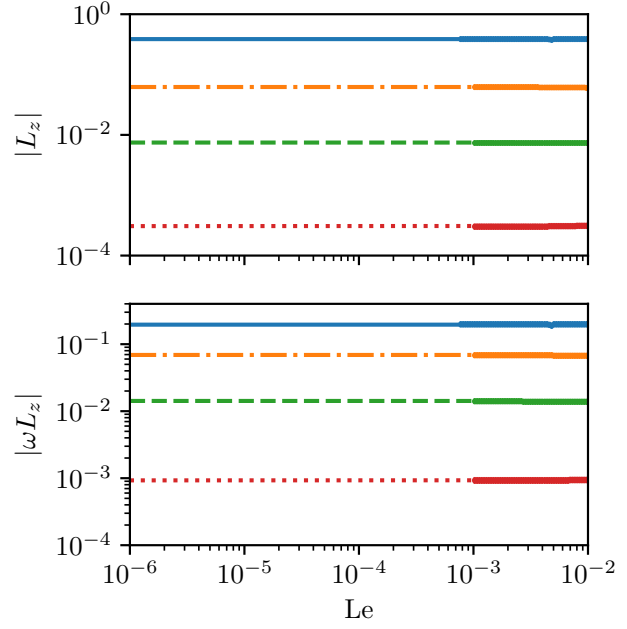


Figure A4. Axial angular momentum (top) and change in axial angular momentum (bottom) for $\mathbf{B}_{0,\text{hyb}}$ and $a, b, c = 1.25, 0.8, 1$ using the hybrid model. The colours correspond to those in Figure A3.